THE ASTROPHYSICAL JOURNAL, 356:591–608, 1990 June 20

HYDRODYNAMIC SIMULATIONS OF STELLAR WIND DISRUPTION BY A COMPACT X-RAY SOURCE

JOHN M. BLONDIN[1] AND TIMOTHY R. KALLMAN
Laboratory for High Energy Astrophysics, NASA/Goddard Space Flight Center
BRUCE A. FRYXELL
Department of Physics, University of Arizona
AND
RONALD E. TAAM
Department of Physics and Astronomy, Northwestern University
Received 1989 August 30; accepted 1989 December 22

ABSTRACT

We present two-dimensional numerical simulations of the gas flow in the orbital plane of a massive X-ray binary system, in which the mass accretion if fueled by a radiation-driven wind from an early-type companion star. We use these simulations to examine the role of the compact object (either a neutron star or a black hole) in disturbing the radiatively accelerating wind of the OB companion, with an emphasis on understanding the origin of the observed soft X-ray photoelectric absorption seen at late orbital phases in these systems. The flow of the stellar wind past the compact star is influenced by a variety of competing effects, including gravitational, rotational, and radiation pressure forces and X-ray heating. Our simulations are characterized by nonsteady accretion wakes at moderate X-ray luminosities ($\sim 10^{36}$ ergs s^{-1}), producing filaments in the downstream wake with densities approaching ~ 100 times that of the undisturbed wind. At high X-ray luminosities ($\gtrsim 10^{37}$ ergs s^{-1}), Compton cooling at small radii results in a steady radial accretion flow onto the compact object. The presence of a photoionization wake, as suggested by Fransson and Fabian, does not contribute significantly to the integrated column density until the wind is X-ray–ionized most of the way to the surface of the companion OB star (requiring high X-ray luminosities and low wind densities). On the basis of these simulations, we suggest that the phase-dependent photoelectric absorption seen in several of these systems can be explained by dense filaments of compressed gas formed in the nonsteady accretion bow shock and wake of the compact object.

Subject headings: hydrodynamics — stars: accretion — stars: winds — X-rays: binaries

I. INTRODUCTION

Of the cosmic X-ray sources, those consisting of a binary system with an OB supergiant in orbit with a collapsed companion, either a neutron star or a black hole, were among the first discovered and are among the best studied. These massive X-ray binaries (MXRBs) are important for our understanding of the late stages of evolution of massive stars and the birth and spin-up of pulsars, and as probes of the properties of single massive stars.

Compared with other phenomena and classes of objects which have been studied in X-rays, MXRBs have a long observational history, and the general properties of their behavior are well established. Many of these properties are consistent with a simple model in which the X-ray emission arises from material that has been captured by the compact object from the strong stellar wind of the primary star. The X-ray source luminosities are generally consistent with this idea, based on the assumption of a spherically symmetric wind and the wind mass flux and velocity law characterizing single OB supergiants. Davidson and Ostriker (1973) obtained an estimate for the fraction of the stellar wind mass flux that is accreted onto the compact object by assuming that all the gas that passes within the accretion radius, $r_{\rm acc} = 2GM/v_{\rm rel}^2 = 2.6 \times 10^{10} v_{\rm rel,8}^{-2} M/M_\odot$ cm, where M is the mass of the accreting object and $v_{\rm rel,8}$ is the relative velocity of the wind in units of 10^8 cm s^{-1}, is captured by the compact object (Hoyle and Lyttleton 1939; Bondi and Hoyle 1944). The resulting theoretical mass accretion rate is given by

$$\dot{M}_{\rm acc} \approx \frac{(GM)^2 \dot{M}_w}{D^2 v_{\rm rel}^4}, \quad (1)$$

where D is the binary separation and $\dot{M}_w$ is the wind mass-loss rate from the primary. This estimate is consistent with the X-ray luminosities of several MXRBs (White 1985), but the strong dependence on the relative velocity makes such conclusions highly sensitive to assumptions about the wind velocity in the vicinity of the compact object. In some objects the estimated wind-supplied accretion rate falls far short of that needed to account for the X-ray luminosity (Conti 1978), implying augmentation by atmospheric Roche lobe overflow (Savonije 1983), X-ray feedback (Ho and Arons 1987*a*), or some other mechanism (Friend and Castor 1982). The photoelectric absorption of X-rays (as evidenced by the turnover in the X-ray spectrum below ~ 1–2 keV) averaged over the binary orbit is generally consistent with that expected if the absorption is due to the primary's wind (White 1985). In systems in which the collapsed object is a pulsar, the rate at which the pulse period changes may be consistent, in some cases, with the transfer of angular momentum to the pulsar from the accreting stellar wind (e.g., Wang 1979, 1981; see also Ho *et al.* 1989).

Hints that the simple model consisting of accretion from a spherical wind is not a complete description of MXRBs come

[1] NAS/NRC Resident Research Associate.

from the discovery that the amount of photoelectric absorption of X-rays is found to be systematically greater at certain phases of the binary orbit than at others (White 1985; Kallman and White 1982; Watson and Griffiths 1977; Charles *et al.* 1978; Branduardi, Mason, and Sanford 1978). Also, systems with an X-ray pulsar undergo episodic changes in the sign of $\dot{P}$, the pulse period derivative (e.g., Boynton *et al.* 1984). Some systems appear to alternate between two or more discrete X-ray brightness states (Schreier *et al.* 1976). Such departures from the simple model could be due to a variety of physical effects related to the interaction of the compact object and its X-ray emission with the stellar wind. These include gravitational focusing of the wind by the compact object, X-ray heating and ionization of the wind, X-ray radiation pressure on the wind, X-ray heating of the primary's surface, and tidal deformation of the primary.

Of the various physical effects which complicate the simple model of MXRBs, each has been investigated individually and suggested as an explanation of certain observed properties. Gravitational focusing of the wind is expected to produce a tail or wake which trails the compact object in its orbit, and which may be responsible for absorption dips observed near phase 0.5–0.6 (inferior conjunction) in some systems (e.g., Jackson 1975). Close to the compact object the accretion flow may be nonsteady, leading to episodic changes in the mass accretion rate and in the specific angular momentum of the accreted material (Matsuda, Inoue, and Sawada 1987, hereafter MIS; Taam and Fryxell 1988). Tidal distortion of the primary can cause enhanced wind flux along the line of centers even if the primary does not fill its Roche lobe (Friend and Castor 1982). X-ray photoionization of the wind can act to suppress or enhance the radiation pressure responsible for the wind acceleration by changing the concentrations of the various ions which absorb the UV from the primary star. If so, the accretion rate will differ from the simple model depending on whether the net radiation pressure force is greater or less than that of a non–X-ray–ionized wind. This can lead to a two-state behavior of the X-ray luminosity: a low state in which X-ray ionization is unimportant and a high state in which the accretion rate is enhanced by the slowing of the wind from X-ray ionization (MacGregor and Vitello 1982; Ho and Arons 1987*a*). In the high-luminosity state shocks may form at the boundary of the X-ray "Strömgren zone" as accelerated wind overtakes the unaccelerated gas within the zone (Fransson and Fabian 1980), possibly producing enough column density in the shocked material to enhance the X-ray absorption.

All of the past work on MXRB gas flows has been limited by simplified assumptions about the equation of state of the gas or about its geometrical configuration. However, many of the characteristics of the flow, in particular those which cause departures from the simple spherical model, are determined on length scales comparable to the orbital separation, and as such they are inherently two- (or three-) dimensional. Furthermore, all the various processes affecting the wind dynamics can interact with each other, producing a situation which is more complicated than the sum of the various simplified models. In this paper we attempt to account for these effects by constructing two-dimensional hydrodynamic models which incorporate many of the physical processes discussed above. We focus on the behavior of the flow on length scales comparable to the binary separation; our goal is to prove the origins of the increased absorption at late orbital phases. In § II we provide some background on MXRBs and describe our numerical method. In § III we present numerical simulations and discuss the effects on the wind of the secondary gravity, X-ray ionization, and X-ray heating. We present a discussion of our results as applied to known properties of wind-fed MXRBs in § IV, and a brief summary in § V.

II. THE MODEL

To investigate the gasdynamics in wind accreting MXRBs we have constructed a simple model that incorporates several of the physical processes in MXRBs that have been previously discussed in the literature. Our method improves on previous models by combining these effects and including them in a two-dimensional simulation. A schematic view of an MXRB, consisting of a gravitating object in a circular orbit with a high-mass companion star of radius R_* and binary separation D is shown in Figure 1 (our convention throughout this paper will be to use capital letters to refer to distances measured from the center of the primary and small letters for distances measured from the compact object). The high-mass star is assumed to corotate with the orbital frequency of the compact companion and to emit a radiation-driven wind that moves out radially from the primary. A fraction of the wind is focused by the gravitational force of the compact object and shocked in an accretion bow shock. The compact object is assumed to emit a constant (accretion-driven), isotropic X-ray luminosity that both heats and photoionizes the wind, creating an X-ray "Strömgren zone" of highly ionized gas. A detailed description of each of these model components (stellar wind, X-ray heating, photoionization) and the numerical technique is given in the following subsections.

a) The Wind

In the absence of Roche lobe overflow, the mass transfer in MXRBs is fueled by a strong stellar wind driven by the radiation pressure from the photosphere of the primary. In the absence of any X-ray ionization, this radiative driving force produces a velocity profile approximated by $v_w = v_\infty(1.0 - R_*/R)^\beta$ in a steady state, where $\beta \approx 0.8$ (Friend and Abbott 1986; Pauldrach, Puls, and Kudritzki 1986). The observed terminal velocity of the wind, v_∞, is approximately 3 times the escape velocity from the surface of the star, v_{esc}, corrected for the effect of continuum radiation pressure (Abbott 1982). The

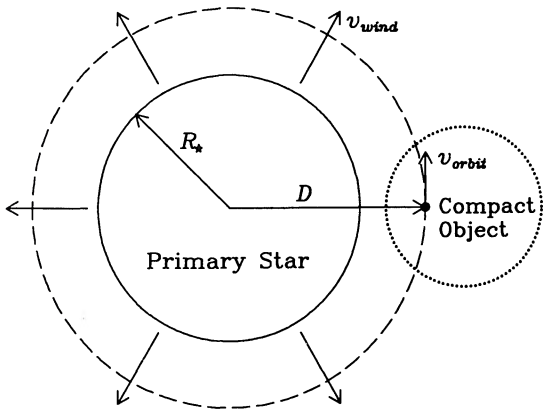

FIG. 1.—Assumed geometry of a wind-fed MXRB with a compact object orbiting counterclockwise around the primary star with velocity v_{orb}. The orbit of the compact object is marked by the dashed line. A spherically symmetric wind is driven off the primary star and is photoionized within an X-ray Strömgren zone (*dotted line*) that surrounds the compact object (*filled circle*).

primary stars in MXRBs typically have masses $M_* \geq 10\ M_\odot$ and radii $R_* \geq 10^{12}$ cm, producing $v_\infty \geq 1000$ km s^{-1}. Typical wind mass-loss rates are consistent with driving by radiation pressure, and approach the single scattering limit imposed by momentum conservation: $\dot{M}_w \leq L_*/(v_\infty c) = 5 \times 10^{-7}\ M_\odot$ yr^{-1} $L_{*38}\ v_{\infty 8}^{-1}$, where L_{*38} is the stellar luminosity in units of 10^{38} ergs s^{-1} and $v_{\infty 8}$ is the wind terminal velocity in units of 1000 km s^{-1}.

In order to simulate the radiation pressure force that drives this stellar wind, we use the Sobolev approximation, incorporating the effects of a finite disk (Friend and Abbott 1986), given by

$$\mathscr{F}_{\rm rad} = \frac{\sigma_e L_*}{4\pi c R^2}\, k K_{\rm fdc} \left(\frac{1}{\sigma_e \rho v_{\rm th}} \frac{dv}{dR} \right)^{\alpha}, \qquad (2)$$

where σ_e is the electron scattering coefficient and ρ and v are the density and velocity of the wind, respectively. The finite disk correction factor is given by

$$K_{\rm fdc} = \frac{(1+\sigma)^{1+\alpha} - (1+\sigma\mu^2)^{1+\alpha}}{(1+\alpha)(1-\mu^2)\sigma(1+\sigma)^{\alpha}}, \qquad (3)$$

with $\sigma = (d \ln v / d \ln R - 1)$ and $\mu = (1 - R_*^2/R^2)^{1/2}$. The finite disk correction is included in order to produce a shallower velocity law ($\beta \approx 0.8$ rather than $\beta \approx 0.5$) and a higher terminal velocity ($v_\infty \approx 3 v_{\rm esc}$), in agreement with observation (Friend and Abbott 1986). The thermal velocity of the gas is $v_{\rm th}$, and k and α are constants representing the number and strength of the absorption lines (Castor, Abbott, and Klein 1975). We have used values of $v_{\rm th}$, k, and α appropriate to single-star winds, while accounting for X-ray photoionization by setting $k = 0$ in the presence of a strong X-ray flux (see § II*b*). When dv/dR becomes negative, we assume that the absorption lines in the wind are completely shadowed from the primary flux and the radiation force is set to zero.

The use of the force law (2) is correct only in the Sobolev approximation, i.e., when the length scale characterizing the flow velocity gradient exceeds the length scale characterizing the ion distribution. More accurate modeling of the dynamics of OB star winds is complicated by the fact that the exact radiation pressure force is known to be unstable to perturbations in the velocity, particularly in the case when the driving lines are optically thin (Owocki and Rybicki 1984; Abbott 1982; MacGregor, Hartmann, and Raymond 1979; Lucy and White 1980; Lucy 1984; and references therein). The growth of these instabilities can produce regions in the wind whose density and/or temperature differ greatly from those predicted by theory based on the Sobolev approximation. However, since models for the nonlinear growth of this instability indicate that the inhomogeneities do not greatly change the *average* wind properties (see Owocki, Castor, and Rybicki 1988), we have chosen to restrict ourselves to the Sobolev approximation in the work reported in this paper.

b) X-Ray Ionization and Heating

The X-ray luminosity emitted by the accreting compact object can strongly influence the dynamics of the wind via X-ray heating and photoionization. X-ray photoionization can inhibit the wind acceleration by changing the line transitions available to absorb the momentum flux from the primary (e.g., MacGregor and Vitello 1982). The radiative acceleration of the wind from the primary occurs because of the existence of many UV line transitions in the gas that are able to capture the momentum flux in the luminosity of the primary. At sufficiently high levels of ionization the most abundant ions have most of their line transitions in the X-ray spectral range. However, the momentum flux from the primary is radiated in the ultraviolet, so there will no longer be a significant overlap in frequency between the wind opacity and the photon flux from the primary star. Thus, within a certain distance from the X-ray source, the wind will be "bleached" of the line transitions necessary for radiative acceleration, and the radiation force on the gas will be reduced within this X-ray Strömgren zone.

The exact manner in which the radiative acceleration is quenched by X-ray photoionization is complicated, owing to the large number of ions and line transitions which can contribute to the UV opacity (e.g., Abbott 1982; Stevens and Kallman 1990). A reasonable approximation for the behavior of the opacity and of quantities associated with X-ray ionization is as follows: For most of the wind the ionization and recombination time scales are shorter than the relevant flow time scale (cf. Fransson and Fabian 1980), so that the gas is locally in ionization equilibrium. If so, the temperature and ionization state depend only on the shape of the X-ray spectrum and on the "ionization parameter," the ratio of the X-ray flux, F_x, to the gas density, n (we adopt the definition $\xi = 4\pi F_x/n$; Tarter, Tucker, and Salpeter 1969). Then we can define some critical ionization parameter, $\xi_{\rm cr}$, above which the Sobolev force is suppressed, and below which the force is unaffected by X-rays. The scaling of wind ionization with ionization parameter is correct only in regions where the wind is optically thin. As shown by Masai (1984), this assumption is not correct for MXRB winds at the boundary of the zone containing He III. In fact, the effects of X-ray absorption cause this zone to be smaller by a factor $\simeq 8$ than it would be if the wind were optically thin. However, as shown by Hatchett, Buff, and McCray (1976), McCray, Wright, and Hatchett (1977) and Kallman and McCray (1982), the ionization structure inside this zone, i.e., at $\xi \geq 10^{1.5}$ ergs cm s^{-1} is not greatly affected by X-ray absorption. It is within this region that the X-ray ionization–related processes of interest occur: radiative driving of the wind is not strongly affected by X-ray ionization unless $\xi \geq \xi_{\rm cr} \simeq 10^2$ ergs cm s^{-1} and X-ray heating affects the dynamics for $\xi \geq 10^3$ ergs cm s^{-1}. Therefore, we feel that the "optically thin" assumption provides an adequate approximation to the effects of X-ray heating and ionization for the purposes of this paper.

The primary effect of the acceleration cutoff will be to lower the wind velocity in the vicinity of the compact object. This will greatly enhance the mass accretion rate onto the compact object because of the strong dependence on velocity (see eq. [1]). Ho and Arons (1987*a*) suggested that this leads to a bimodal behavior of X-ray luminosity: Sources can exist either in a low-luminosity state, in which the X-ray ionization is unimportant in determining the accretion rate, or in a high-luminosity state, where the wind velocity is greatly reduced by this effect. A related effect of the acceleration cutoff is the formation of a dense wake of gas trailing behind the ionized region, where the fast, accelerated wind catches up and collides with the slow, unaccelerated wind that has passed through the Strömgren zone (Fransson and Fabian 1980). The high column density of gas in this photoionization wake may contribute to the photoelectric absorption of the X-rays at late orbital phases.

X-rays can also affect the thermal state of the wind through radiative heating and cooling processes. For ionization param-

eters $\xi \leq 10^5$ ergs cm s^{-1}, X-rays heat the gas via photoionization while radiative losses cool the wind. At greater ionization parameters Compton scattering dominates the radiative processes and either heats or cools the wind, depending on whether the gas temperature is below or above the inverse Compton temperature, $T_{IC} = \langle \epsilon \rangle / 4k$, where $\langle \epsilon \rangle$ is the mean photon energy. This can lead to temperature distributions which differ greatly from those calculated under the assumption of adiabatic flow, and can change the local effective adiabatic index.

c) *The Numerical Model*

The numerical simulations of the gas flow in wind-fed MXRBs presented in this paper were created using a time-dependent gasdynamics code that incorporates the physical effects discussed so far in this section: forces due to the gravity of the primary and compact star and the radiative acceleration of the primary wind, including suppression in the X-ray Strömgren zone, and the influences on the gas temperature of radiative cooling and X-ray heating. The gas flow is calculated only in the orbital plane of the binary system in order to reduce the problem to two dimensions, r and ϕ. We thereby assume no gradients in the polar angle, θ, and no flow in or out of the plane. The computational grid is initialized with a smooth, steady wind, and is allowed to evolve according to the conservation equations as given in the Appendix.

The numerical technique employed is based on an explicit, Eulerian version of the piecewise parabolic method developed by Collela and Woodward (1984) and used to study axisymmetric (Fryxell, Taam, and McMillan 1987, hereafter FTM) and asymmetric (Fryxell and Taam 1988, hereafter FT; Taam and Fryxell 1989, herafter TF) accretion onto a compact object. The force terms in this code include the Newtonian gravity of the primary and compact object, and the radiation force of the primary responsible for accelerating the stellar wind (eq. [2]). To simulate the effects of photoionization, we set this driving force to zero when $\xi > \xi_{cr} = 10^{2.5}$ ergs cm s^{-1} (see § II*b*).

We neglect the radiation force of the X-rays from the compact object. As shown by Buff and McCray (1974), McCray and Hatchett (1975), Hatchett, Buff, and McCray (1976) and others, photoelectric absorption can greatly increase the radiation pressure force relative to that produced by electron scattering. This can affect the Eddington limit for accretion onto an X-ray source, and is most pronounced for gas which is optically thin to X-rays. However, for the conditions appropriate to MXRB winds the radiation pressure force is increased by at most a factor of ~ 3 relative to electron scattering owing to the effects of X-ray absorption and of ionization of the hydrogen and helium in the wind by the primary star. Therefore, we consider our approximation to be justified for X-ray luminosities up to 10^{37} ergs s^{-1}.

The energy sources and sinks are calculated in a separate step from the gasdynamics and are computed under the assumption that the gas is optically thin and in ionization equilibrium with a constant, isotropic X-ray photon flux from the compact object. At each point in the wind, the heating rate Γ due to X-rays and the cooling rate Λ due to X-rays and locally emitted radiation are calculated as a function of temperature T and ionization parameter ξ (Γ and Λ are given in units of ergs cm^3 s^{-1}). We assume that the elemental abundances are cosmic (e.g., Withbroe 1971) and that the X-ray spectrum is a 10 keV bremsstrahlung (see Kallman and McCray 1982 for details of the photoionization calculation). The effects of the primary star are accounted for by not letting the wind temperature drop below the surface temperature of the primary, T_*. Although it is likely that the temperature of the wind from a single star is slightly lower than T_* ($T_w \sim 0.9T_*$; Klein and Castor 1978), the results of our simulations depend only very weakly on this temperature.

The numerical simulations are calculated in the equatorial plane of a spherical grid centered on the primary, so that the radial force that drives the wind and the gravity of the primary can be easily calculated in one coordinate (see Appendix). In addition, this allows us to include the spherical divergence of the wind as it leaves the primary. The orbital velocity of the compact star, v_{orb}, is accounted for by rotating the grid at the angular frequency of the orbit, such that the compact object remains fixed with respect to the computational grid. The computational grid of 250 radial by 200 angular zones extends from 1.0 to 2.7 stellar radii and in angle from -0.6 to $+0.4$ radians, where zero is the line joining the centers of the two stars. The grid spacing is nonuniform, with the zone size decreasing toward the compact object in order to resolve the dynamics of mass accretion that occur on the small length scales associated with the compact object. The smallest zones, near the surface of the compact object, have dimensions of $\Delta R = 1.5 \times 10^{-3} R_*$.

The radial velocity at the surface of the primary is set to zero, and the density there is adjusted to provide the desired wind mass-loss rate. We also set the tangential velocity to zero, corresponding to the assumption of corotation for the primary star. On the other three sides of the grid the gradients of all flow variables are set to zero, permitting the matter to flow freely out of the grid. This technique is satisfactory on the top and right-hand side of the grid (i.e., downstream of the compact object in a frame of reference rotating with the primary), where the flow is always moving supersonically off the grid. On the left-hand side the wind entering the grid is accurate provided that the boundary is outside the region of disturbed wind (i.e., outside the Strömgren zone).

The boundary conditions at the surface of the compact object are restricted by our use of a spherical grid centered on the primary star. In addition, we have limited the spatial resolution near the compact object in order to follow the large-scale dynamics of the mass transfer process for many flow times across the binary separation. If we allow the zone size near the compact object to be arbitrarily small, the corresponding Courant time step would become prohibitively short. Our choice of grid spacing and boundary conditions near the compact object is made to facilitate the study of the large-scale dynamics of the disturbed stellar wind without having to calculate the short time scale dynamics of the mass accretion close to the surface of the compact object. Our treatment of the flow at small radii is verified by the high spatial resolution work of FTM, FT, and TF, who use a finely spaced grid to study accretion onto a compact star. Before running the full simulations, we tried several runs varying the shape and resolution (number of zones) near the compact object, which demonstrated that, qualitatively, the large-scale flow does not depend strongly on the shape or resolution of the inner boundary. We therefore adopted the simplest approach, using a box of 3 zones by 3 zones within which the normal velocity (but not the total energy) is set to zero at each time step. This is similar to the intermediate boundary condition applied at the spherical surface of the compact star in the calculations of FTM.

TABLE 1

MODEL PARAMETERS

Parameter	Symbol	Value
Mass of primary	M_*	$23\ M_\odot$
Radius of primary	R_*	2.5×10^{12} cm
Effective temperature of primary	T_*	40,000 K
Wind mass-loss rate	$\dot{M}_w$	$4 \times 10^{-6}\ M_\odot\ \mathrm{yr}^{-1}$
Terminal wind velocity	v_w	1700 km s^{-1}
Mass of compact object	M_{co}	$1.4\ M_\odot$
Binary separation	D	$1.5R_*$
Orbital period	P_{orb}	9.3 days
X-ray luminosity	L_x	5×10^{36} ergs s^{-1}
Effective temperature of X-ray flux	T_x	10 keV

Because of this crude approximation, the dynamics within a few zones of the compact object (i.e., $r \ll r_{acc}$) are not well resolved. We do not consider this a serious flaw in our calculations, because the true boundary conditions at the accretion surface (e.g., the magnetosphere) of a compact object are extremely uncertain.

III. RESULTS

The flow of a stellar wind past a gravitating compact object in MXRBs is complicated by the interaction of several competing processes. In an attempt to isolate and understand the importance of each of the physical effects that influence the gas flow in MXRBs, we present several idealized models in which only a specific subset of the physics discussed in the previous section is included. In this section we use these restricted simulations to discuss separately the effects of gravity, X-ray photoionization, and X-ray heating. We then examine the full simulations that incorporate all of the physics available in our numerical model and use them to explore a limited parameter space of observed MXRBs. The system parameters chosen for our standard model are given in Table 1, and have been chosen in accordance with the inferred parameters of Vela X-1 (4U 0900−40).

a) Gravity

Our first simulation is of a strictly adiabatic, smoothly accelerating wind from a corotating primary in which the only influence of the compact object on the gas flow is via its gravity. This simulation should come closest to the approximation of uniform, axisymmetric accretion (although our calculation is only in two dimensions). For an ideal gas with an adiabatic index of $\gamma = 5/3$, the focusing of the stellar wind will lead to the formation of a standing bow shock at a distance of $\sim r_{acc}$ in front of the compact object, with the "wings" of the bow shock forming an extended wake downstream (e.g., Hunt 1971; Shima *et al.* 1985; FTM). A halftone display of the density distribution in the orbital plane is shown in Figure 2. The stellar wind approaches the compact object at a slight angle with respect to the line of centers, which we shall refer to as the accretion angle, $\theta_{acc} \approx 11°$. Although the Coriolis force bends the accretion wake slightly behind the compact object, there is a roughly axisymmetric accretion cone extending far downwind from the compact object. The accretion radius in this simulation is only 7×10^{10} cm and so is not visible on the scale of this plot, and the Mach number of the wind relative to the compact object at the bow shock is $\mathcal{M}_{bow} = 30$. The compression of the wind in the bow shock is a factor of 4 (the high Mach number limit for $\gamma = 5/3$), with further compression as the flow converges onto the compact object. The shock compression in the wings of the bow shock is only a factor of 2 because the shock front becomes very oblique downstream from the star. The total integrated density along the line of sight produces an enhancement of a factor of ~ 1.5 in the column density around phase 0.5 (Fig. 3). This falls far short of that needed to explain observed absorption variations (see § IV). After the wake leaves our computational grid, the Coriolis force continues to wrap it back around the primary, so the double-peaked structure in Figure 3 is likely to be smeared out. On the basis of this simulation we do not expect the excess in the column density to appear at orbital phases much later than ~ 0.6 unless the assumption of corotation is relaxed and the wind is much slower than assumed near the primary.

The "ripples" seen in the accretion wake in Figure 2 are a result of the nonzero angular momentum in the accreting stellar wind with respect to the compact object. The axisymmetry of the accretion flow is broken by the orbital velocity of the system, even for a corotating companion. Because the wind approaches the compact object at a finite angle with respect to

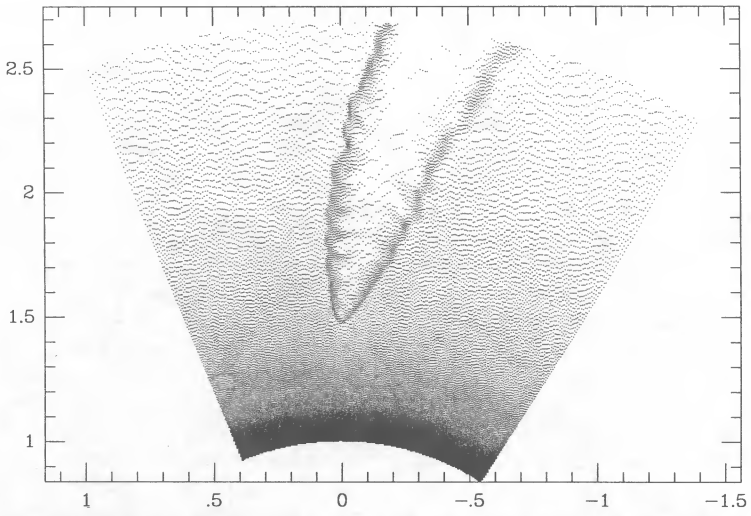

FIG. 2.—Accretion wake of a compact object in an adiabatic, continuously accelerated stellar wind. The halftone scale displays the density of the wind from 10^9 cm^{-3} (*white*) to 10^{11} cm^{-3} (*black*). The physical dimensions of this and the following plots are labeled in units of stellar radii, $R_* = 2.5 \times 10^{12}$ cm. The compact object is located at coordinates (0, 1.5), near the apex of the bow shock. The accretion radius is 7×10^{10} cm, or 0.028 in the normalized units.

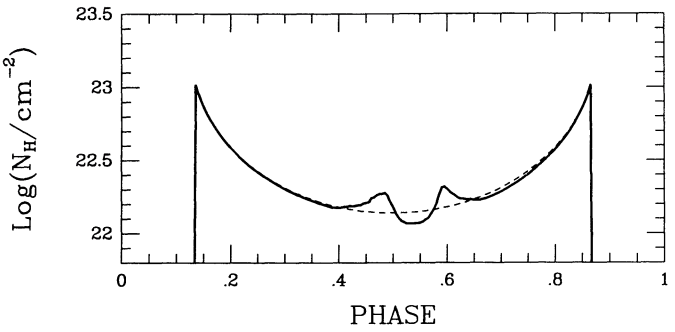

FIG. 3.—Line-of-sight column density, N_H, as a function of orbital phase for the adiabatic wind simulation shown in Fig. 2. The dashed line is the column density expected for a spherically symmetric, undisturbed wind. The solid line is the column density derived from the simulation results and averaged over several time steps. We have assumed that the density of the wind outside the computational grid is given by that of the undisturbed wind, and hence have underestimated the deviation from a smooth wind at phases where the wake extends beyond the grid.

the line of centers, the wind on the trailing side of the compact object (lagging behind in orbit) is closer to the primary and therefore denser than the wind on the leading side owing to the $1/r^2$ divergence of the wind (see Fig. 1). Initially, the asymmetry in the flow leads to a larger ram pressure on the high-density side that drives the bow shock off toward the low-density side. As the bow shock swings over to this side, it begins to intercept more of the wind from this side than from the high-density side, and is eventually pushed back to the high-density side, where the whole process repeats itself in a quasi-periodic fashion (see FT).

The structure of the accretion wake on scales $\gtrsim r_{acc}$ is qualitatively similar to the higher resolution simulations of FT with comparable density asymmetries. In particular, we find that the accretion wake flips from one side to the other on the time scale of the flow time across the accretion diameter, $2r_{acc}/v_{rel} \approx 10^3$ s. However, we do not find extended periods ($\sim$1–2 flow times) in between the transition states corresponding to the formation of a disklike structure at small radii. As a result, the oscillation period in our simulations is only $\sim$2 flow times, as opposed to $\sim$4 flow times in the corresponding simulation of FT. This difference may arise from the larger Mach number in our simulation, which can lead to a narrower accretion wake and hence smaller amplitude oscillations (TF). However, based on our experience with the effects of numerical resolution, we may simply be unable to resolve the accretion flow sufficiently at small radii (we have approximately 12 grid zones across the accretion radius in this simulation).

The gravitational potential of the compact star can also affect the wind mass-loss rate from the primary. The mass-loss rate is enhanced along the line of centers of the binary system via two related effects. The first effect is the tidal distortion of the primary, which lifts the base of the wind farther away from the center of the primary in the direction of the compact object. The second, related effect is the weaker gravitational force along the line of centers, such that the wind is "fighting" less gravity in this direction. Friend and Castor (1982) found that the mass-loss rate was strongly enhanced even when the primary was well within its critical potential lobe. They suggested that as the radius of the primary approached the critical surface, this enhanced wind becomes Roche lobe overflow. Petterson (1978) has claimed that, for some binary parameters, this "gas stream" will have insufficient orbital angular momentum to catch up with the orbiting compact object, and will simply fly off behind the star. This gas stream could then be observable in the phase-dependent absorption of X-rays (Haberl, White, and Kallman 1989). Our simulations do not address this problem because we force the stellar surface of the primary to be spherical. We do, however, treat the binary potential correctly, and find a modest (10%) increase in wind velocity along the line of centers as compared to 30° off-center. Because of our restriction on the shape of the primary, the density is actually less along the line of centers and the wind mass-loss rate is only $\sim$3% greater, in contrast to the 20% increase determined for Vela X-1 by Friend and Castor (1982). Future work with this code will incorporate the boundary conditions needed to model this gas stream accurately.

b) X-Ray Photoionization

The simple model of a uniform stellar wind accreting onto a compact object will be altered by the accretion-driven X-ray flux that will photoionize the wind within an X-ray Strömgren zone surrounding the compact object. To separate the effect of photoionization in producing a wake of compressed gas from the wake associated with the accretion bow shock, we have run a simplified version of our model including X-ray ionization effects but without the compact object gravity, and using a strictly adiabatic gas. The resultant flow should be a smoothly accelerating wind except for a Strömgren zone around the ionizing source, where the radiation force on the wind is suppressed. We then ran an adiabatic version of the model with both a photoionization cutoff and the gravity of the compact object in order to illustrate the effects of X-ray ionization on the accretion wake.

i) *Without Gravity*

This idealized problem can be parameterized in terms of the nondimensional geometric parameter q, which defines surfaces of constant ionization parameter (Hatchett and McCray 1977):

$$q = \xi_{cr} \frac{n(D)D^2}{L_x} = \frac{\dot{M}_w \xi_{cr}}{4\pi \bar{m} v_\infty L_x} \left(1 - \frac{R_*}{D}\right)^{-\beta}, \quad (4)$$

where $\bar{m}$ is the average mass per ion. Estimated values of q (based on L_x inferred from X-ray observations of MXRBs and $\dot{M}_w$ inferred from the UV lines of the primary and similar stars; Conti 1978) are in the range $\sim$0.5–5 (Vela X-1 and 4U 1700−37) and $\sim 10^2$–10^4 (Cyg X-1, Cen X-3, and SMC X-1). The Mach number of the wind represents another independent variable in this idealized problem. However, because any shocks within the wind are very oblique (in the absence of an accretion shock), the structure of the wind is relatively insensitive to the Mach number. Of more importance to the problem is the steady state wind velocity profile. The efffects of a bleached zone are more pronounced for slower acceleration laws (i.e., $\beta = 0.8$ rather than 0.5), where the wind is strongly accelerating for a larger fraction of the distance to the compact star. The simulations described here are only for $\beta \sim 0.8$, as produced by the Sobolev approximation (eq. [2]). Using our standard parameters, the Mach number at the compact object is $\mathcal{M} = 30$ in the undisturbed wind.

Figure 4 shows the photoionization wake for three relatively small values of q. When the wind enters the Strömgren zone, the radiation force is cut off, and this "disturbed wind" coasts with the radial velocity it had when it crossed into the Strömgren zone. When the disturbed wind leaves the Strömgren zone downstream, it is traveling slower than the wind that passed

behind the ionized region. The undisturbed wind that passed behind the Strömgren zone will catch up with and overtake the slower wind. For large values of q (>10) the difference in radial velocities is relatively small and the Strömgren zone has a negligible effect on the stellar wind. The effect of photoionization becomes more pronounced for smaller values of q, where the Strömgren zone reaches deep into the base of the wind. As the Strömgren zone comes closer to the surface of the primary, the difference in radial velocities of the accelerated and the unaccelerated winds becomes larger and larger. For $q \sim 6$ the disturbed and undisturbed winds begin to collide at a very shallow angle, producing a mild compression of the wind outside the Strömgren zone (Fig. 4*a*). For even smaller q the relative velocities become supersonic, and a shock is formed on the inside edge of the wake. The density within the wake can become very large, with a factor of ~ 50 increase over the undisturbed wind in the run with $q = 2.0$ (Fig. 4*c*). As q becomes smaller, the compression of the wind begins to alter the effective Strömgren zone (marked by the solid line in Fig. 4), such that the photoionization wake always reaches within a stellar radius of the compact object. For small values of q the column density of the photoionization wake can become significantly larger than the undisturbed wind. The column density for the simulation shown in Figure 4*c* is a factor of ~ 5 greater than the undisturbed wind at phase 0.75. For very small values of q the photoionization wake wraps around the primary star, and can increase the observed column density at late phases, possibly all the way into eclipse.

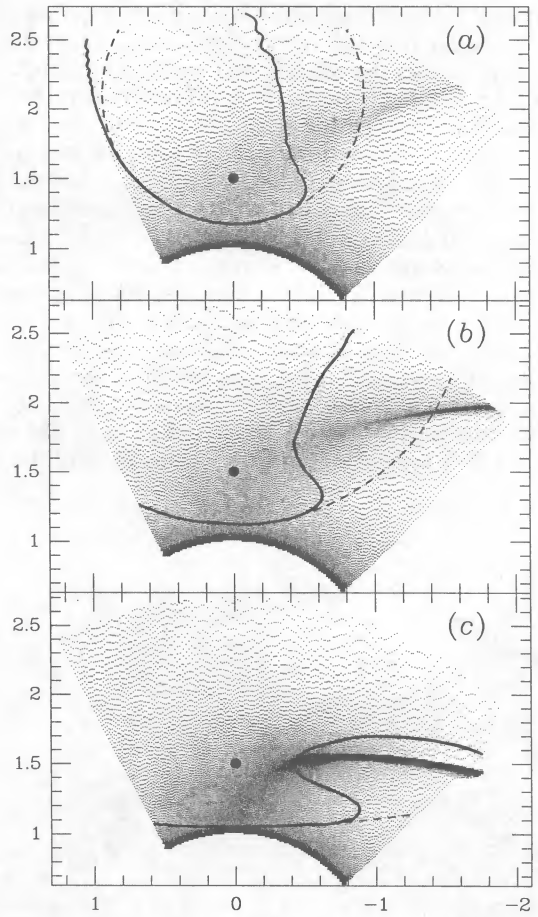

FIG. 4.—Density distribution of the photoionization wake as a function of the size of the X-ray Strömgren zone. The values of q are (*a*) 6.3, (*b*) 4.0, and (*c*) 2.0. The density scale varies from 10^9 cm^{-3} (*white*) to 10^{11} cm^{-3} at saturation (*black*). The location of the X-ray source is marked by a filled circle. The dotted line is the surface of the Strömgren zone in the undisturbed, spherically symmetric wind, and the sold line is the self-consistent Strömgren zone, accounting for the changes in the wind density. A very strong photoionization wake begins to show only for relatively small values of q, where the Strömgren zone reaches close to the surface of the primary.

The presence of the X-ray Strömgren zone produces a low-density rarefaction valley on the leading edge of the zone analogous to the compression wake on the trailing edge. Streamlines near the leading edge that pass through the Strömgren zone move slower and are bent off to the right by the Coriolis force more than the streamlines that pass just outside the ionized region. This leaves a cone of low-density gas trailing off in the wind from the point on the surface of the Strömgren zone that is tangent to the undisturbed wind streamlines.

Note that the accelerating wind may be susceptible to dynamical instabilities in regions where $\xi \sim \xi_{cr}$. A local density enhancement will remain accelerated ($\xi < \xi_{cr}$) while the surrounding gas begins to coast, unaffected by the UV flux from the primary star. The higher density gas will then sweep up the slower material, increasing in density and maintaining $\xi < \xi_{cr}$. Whether or not the wake of compressed gas breaks up into clumps is likely to depend on the details of how the radiation force is quenched by X-ray photoionization. A more accurate treatment of the microphysics is required to determine whether the wind is truly unstable to density perturbations in this region of critical ionization. In such a case we would still be left with a significant enhancement of N_H, but with more variation with orbital phase than seen in our results. This instability is independent of, and in addition to, the instabilities of isolated O star winds (e.g., Owocki and Rybicki 1984).

ii) *With Gravity*

In the presence of gravity, the slower wind in the X-ray Strömgren zone will also have a strong influence on the accretion wake by changing the accretion radius. A small decrease in the relative wind velocity with respect to the compact object can produce a much larger accretion radius and mass accretion rate (see eq. [1]). To investigate the effects of X-ray photoionization and the attendant reduction in the wind driving force on the accretion flow with gravity, we considered another adiabatic simulation, shown in Figure 5. For this and the following simulations we use a critical ionization parameter $\xi_{cr} = 10^{2.5}$ ergs cm s^{-1} to characterize the cutoff of the radiative driving force (cf. § II*b*). With our adopted parameters, this corresponds to cutting off the wind at a distance of $\sim 0.15 R_*$ from the surface of the primary. A comparison with the first adiabatic simulation (Fig. 2) immediately shows a larger accretion cone, corresponding to a larger accretion radius of 2×10^{11} cm. The Mach number of the wind relative to the compact object is $\mathcal{M}_{bow} \approx 16$, and the accretion angle is $\theta_{acc} \approx 21°$.

With this larger accretion radius we were able to resolve the formation of an "accretion disk" inside the bow shock. Although this is not necessarily a true viscous accretion disk, it represents a significant amount of matter circulating around the compact object at approximately Keplerian velocities. The qualitative structure of the flow is similar to the simulation of FT (keeping in mind the differences between our simulations and those of FT) for a density asymmetry of $\epsilon_\rho = 0.0625$, where $\epsilon_\rho(\epsilon_v)$ denotes the ratio of the axisymmetric accretion radius to

the length scale of the density (velocity) variation across the accretion cylinder. For comparison, we estimate density and velocity asymmetries of $\epsilon_\rho \sim 0.11$ and $\epsilon_v \sim -0.047$ in our simulation, with the high-density side corresponding to the low-velocity side.

The temporal behavior of our adiabatic simulation is different from that found in the simulations of FT. Whereas FT observed a continually oscillating disk/wake structure, we have followed the evolution for ~ 35 flow times (the flow time across an accretion diameter for this simulation is $\sim 10^4$ s) and have not observed any change in the disk rotation. The extended side of the accretion wake remained on the high-density side of the compact object, feeding a disk circulating in the counter sense; the rotation is opposite to that of the binary orbit, and hence the accreted angular momentum is negative. This quasi-steady flow configuration is qualitatively similar to the simulation of MIS for $\gamma = 5/3$ and a sound speed of $c_0 = 2$ at the surface of the mass-losing star. The simulation of MIS also possessed a steady, counterrotating disk. When MIS increased the sound speed in their models, the flow began to oscillate, which we suspect is a result of the decreased numerical resolution behind the bow shock owing to the decrease in the accretion radius. Similarly, our previous simulation (Fig. 2) may not show this steady behavior for the same reason: inadequate spatial zoning to resolve the steady state flow pattern.

The density and velocity structure of this quasi-equilibrium flow is shown in Figure 6. The steady nature of the flow appears to arise from a balance between the ram pressure of the wind trying to push the accretion column back behind the compact object and the high thermal pressure of the wake interior. This interior pressure is supplied by the accreting gas which approaches the compact object along the accretion column and passes close to the star on the side of the primary, thus feeding the circulating flow in a counter sense. As the accretion flow comes around the compact star, it is heated in at least one spiral shock. The shock-heated gas provides thermal pressure support, pushing on the accretion column from the back side and balancing the ram pressure of the wind from the front side.

After ~ 25 flow times, this quasi-steady structure disappeared for approximately 7 flow times as the shock-heated gas behind the compact object began to circulate inside the old accretion disk in the same sense of rotation. Although the flow at this time is unsteady, it is not the same as the oscillating flow seen by FT because the accreting gas is always circulating around the compact object in the same direction. During this time the flow near the compact object is a complicated interaction of several spiral shocks and concentric "disks." During this time the large-scale wake reflects the unsteady flow at small radii and appears rippled and more symmetric. This behavior is shown in Figure 7, which shows a series of snapshots of the flow starting at 2×10^5 s and separated in time by 2×10^4 s (~ 2 flow times). Eventually the accretion flow settled down to its original steady configuration with the extended wing on the high-density side of the compact object. Both the multiple spiral shock behavior and the quasi-steady flow differ from those of FT, who found a continually oscillating disk/wake structure. This difference may be attributed to the higher Mach number in our simulation, the presence of a standoff bow shock (a result of the partially reflecting inner boundary and $\gamma = 5/3$ rather than $\gamma = 4/3$), or the combination of a density and velocity gradient. A more likely explanation is the stiffer equation of state in our simulation, which allows for higher pressures in the converging fluid flow near the compact object. These higher pressures may prevent the ram pressure of the wind from pushing the accretion wake to the low-density side, resulting in the quasi-steady flow pattern seen in Figure 6.

The high-density wing of the accretion wake on the trailing side of the compact object contributes significantly to the integrated column density at late phases, $\phi_{\rm orb} \sim 0.7$–0.8, as seen in Figure 8, which displays an average of the integrated line-of-sight column density of the compact object as a function of orbital phase. Some of the structure seen in this plot is variable with time as the wake bounces mildly and the vortices within the wake are advected downstream, but the large enhancement around $\phi \sim 0.7$ remains relatively constant. This secondary peak in column density will be shifted to later phases if the primary is not corotating or if the acceleration of the wind is

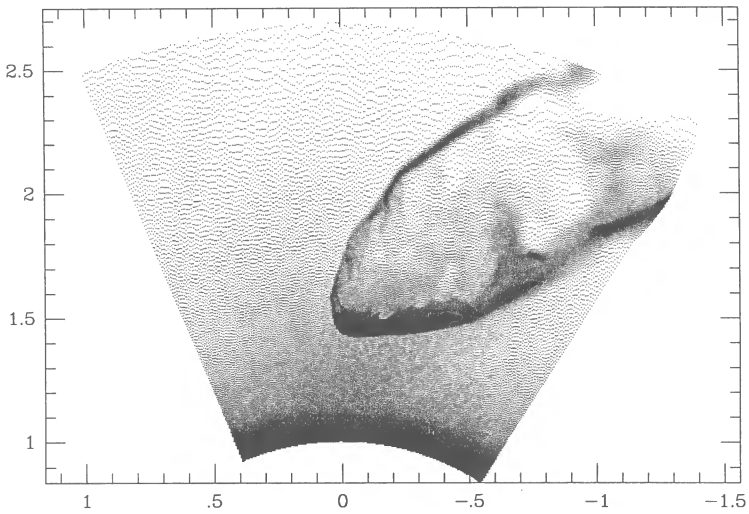

FIG. 5.—Accretion wake of a compact object in an adiabatic wind whose velocity has been diminished by the photoionization effects of the X-rays emitted by the compact object. The density scale is the same as in Fig. 2. The X-ray luminosity produces a Strömgren zone characterized by $q \approx 6$, which reduces the wind velocity at the compact object by a factor of ~ 2.

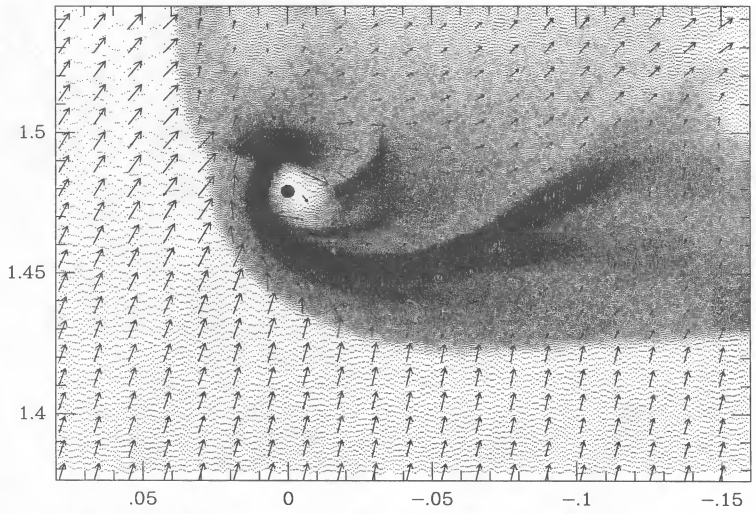

FIG. 6.—Magnified view of the accreting stellar wind in the adiabatic simulation shown in Fig. 5. The density scale now runs from 3×10^{10} cm^{-3} to 5×10^{11} cm^{-3} at saturation. The location of the compact object is marked by the filled circle. The vectors display the velocity field of the accreting wind, with the length of the vectors scaled to the absolute velocity. Here the maximum velocity corresponds to 1.3×10^8 cm s^{-1}. The accreting stellar wind is first slowed in the bow shock, and then approaches the compact object along an accretion column that terminates in a strong shock on the back side of the star. Additional spiral shocks can be seen in the vicinity of the compact object.

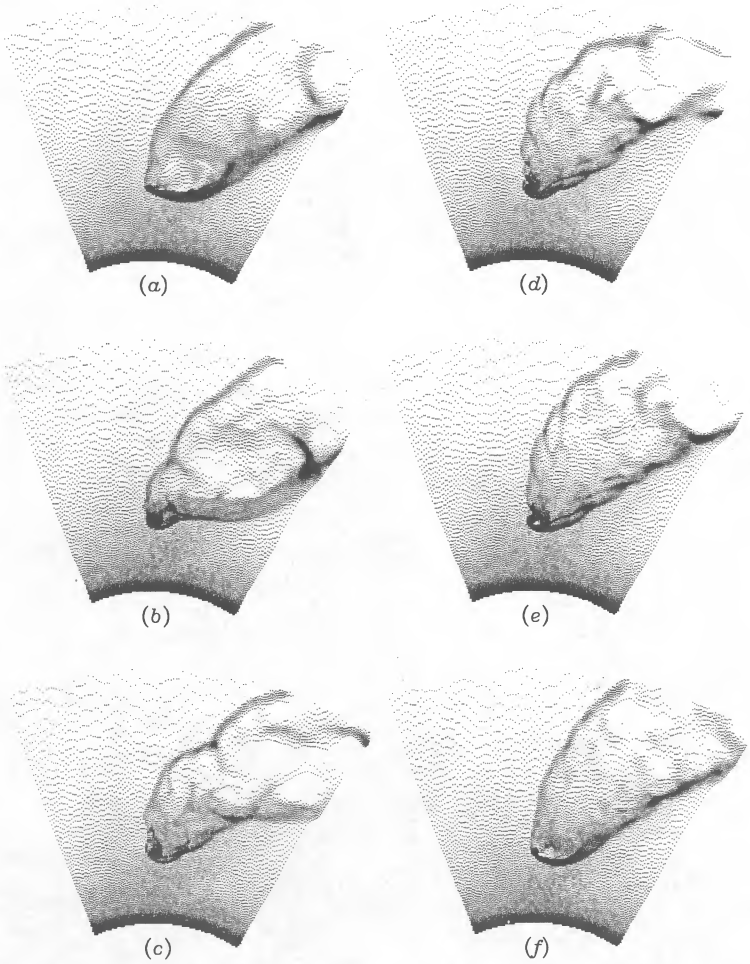

FIG. 7.—(*a*–*f*) Series of six "snapshots" from the adiabatic simulation shown in Figs. 5 and 6. Each image is separated in time by ~2 flow times across an accretion diameter. The halftone scale displays the density of the wind as in Fig. 2. The flow remained relatively steady up until the time shown in the first frame, after which the wake is fed by a rapidly rotating, multiple disk structure. By the last frame the accretion wake had settled back into the quasi-steady structure observed for the first 25 flow times (compare [*a*] and [*f*]).

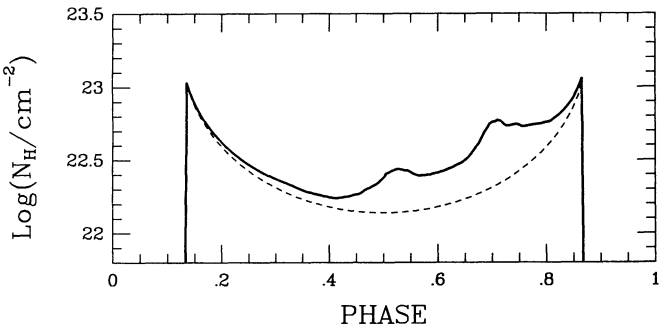

FIG. 8.—Same as Fig. 3, but calculated for the adiabatic simulation shown in Fig. 7. The solid line is the integrated column density averaged over the first 25 flow times.

cut off even closer to the surface of the primary. Alternatively, a smaller value of β in the wind velocity profile will shift this peak to earlier phases.

c) *X-Ray Heating*

One of the most intriguing results of our simulations is the important role played by X-ray heating and radiative cooling in determining the temporal behavior of the accretion flow. The strongest heating and cooling occur close to the compact object, where the Compton time scale is relatively short, although X-ray heating can also affect the wind at larger radii by lowering the Mach number. In the presence of a strong X-ray source, X-ray heating could actually disrupt the flow and induce shocks if the heating were sufficient to raise the local sound speed above the velocity of the wind (e.g., Cowie, Ostriker, and Stark 1978). To do this requires not only a high equilibrium temperature (so that $\mathcal{M} \lesssim 1$) but also a heating rate that is sufficiently rapid that the heating time, $t_h = kT/n\Gamma$, is less than the flow time, $t_{fl} = r/v$.

Outside the accretion radius the X-ray flux cannot disrupt the flow because the wind remains supersonic for typical MXRBs. If we estimate the equilibrium temperature as $T_{eq} \approx 10^3\ \xi$ (cf. Kallman and McCray 1982), the Mach number of the wind decreases as the wind approaches the compact object owing to the increased X-ray flux. The minimum Mach number for $r > r_{acc}$ is therefore at r_{acc}. Using the wind velocity law with exponent $\beta = 0.8$, the Mach number at the accretion radius is

$$\mathcal{M}_{acc} \approx 3.0\left(\frac{\dot{M}_w}{10^{-6}\ M_\odot\ \mathrm{yr}^{-1}}\right)^{1/2}\left(\frac{L_x}{10^{36}\ \mathrm{ergs\ s}^{-1}}\right)^{-1/2} \times \left(\frac{v_\infty}{10^8\ \mathrm{cm\ s}^{-1}}\right)^{-3/2} \quad (5)$$

Thus, unless the X-ray luminosity is very high relative to the wind mass-loss rate, the wind will remain supersonic through the accretion radius. When the wind velocity is reduced by photoionization effects, the larger wind density results in a cooler wind and hence higher Mach number, requiring an even higher X-ray luminosity to disrupt the flow.

Inside the accretion radius the Compton time is longer than the inflow time, and again X-ray heating cannot disrupt the accretion flow. If we assume that the heating rate is dominated by Compton heating (a reasonable assumption if heating is going to disrupt the flow), the heating time scale is given by $t_h \approx 4\pi m_e c^2 r^2/m_p \sigma_e L_x$. Comparing this with the free-fall flow time past the compact object, $r/v_{ff}(r)$. we find that Compton heating is sufficiently fast to raise the temperature only within a radius $r_h \approx 10^9 L_{37}^2$ cm. Unless the X-ray luminosity approaches the Eddington limit, $r_h \ll r_{acc}$. Upon passing the accretion bow shock, however, the velocity will be reduced below free fall, increasing the flow time and allowing Compton heating to have more of an effect. For typical MXRB systems, X-ray heating cannot induce shocks on its own, although we will see later that Compton processes can be very important *inside* the accretion bow shock.

Note that at very small radii, $r \lesssim 6 \times 10^{10}$ cm, where adiabatic heating acts to raise the gas temperature above T_{IC}, Compton scattering will cool the accreting gas. For moderately high X-ray luminosities, $L_x \gtrsim 10^{37}$ ergs s^{-1}, Compton cooling will be fast enough to keep the flow roughly isothermal, with the gas temperature fixed at T_{IC}. This cooling effect is important in our simulations only within a few times 10^{10} cm of the compact object, and yet it may be responsible for dramatic differences in the temporal behavior of our simulations.

The overall effect of X-ray heating and radiative cooling is best shown by comparing the adiabatic simulation of Figure 5 with the full model shown in Figure 9, the only difference between these being the X-ray heating and radiative cooling in the latter run. Although the detailed structure near the compact object is very similar in these two flows at this particular instant (compare Figs. 6 and 10), the full simulation is clearly not as steady as the adiabatic simulation. The extended wake of the run with X-ray heating is highly asymmetric as a result of oscillations in the disk/bow shock structure, similar to that seen in the simulations of FT and TF. The effects of X-ray heating that cause this gross change in behavior are rather subtle, for the dynamics near the compact object remain very similar. One effect of X-ray heating is the change in the Mach number of the stellar wind at the bow shock, from $\mathcal{M}_{bow} \sim 25$ in the adiabatic run to $\mathcal{M}_{bow} \sim 2.8$ in the X-ray–heated run. From the simulations of TF, a higher Mach number flow will produce a narrower wake and hence weaker oscillations from side to side. The similarity of the bow shock in these two flows, and the comparable postshock temperatures and pressures, suggest that the difference in Mach number is not sufficient to explain the striking difference in flow behavior. Another influence of radiative heating and cooling is to change the effective adiabatic index of the gas, particularly inside the accretion bow shock. For the parameters used in these simulations, the Compton time scale is roughly 10^3 s, comparable to the flow time inside the bow shock. Compton scattering will act to keep the temperature at T_{IC}, lowering the effective adiabatic index. This explanation is consistent with the fact that FT found disk oscillations in an asymmetric flow with $\gamma = 4/3$, while we observed oscillations in an X-ray–irradiated (approximately isothermal) flow but not in an adiabatic flow with $\gamma = 5/3$. The results of MIS may also support this explanation: for their simulations with $c_0 = 1.5$ they found a steady flow for $\gamma = 5/3$, while the wake "flip-flopped" for $\gamma = 4/3$. Note, however, that their results may be affected by poor spatial resolution, particularly for the higher wind speeds.

d) *Full Model*

The time-dependent nature and asymmetry of wind-fed MXRBs is revealed in the complete simulation incorporating gravity, photoionization, and X-ray heating and cooling (Fig. 9). The "sheets" of dense gas in the accretion wake can be found on either side of the compact object as a result of the

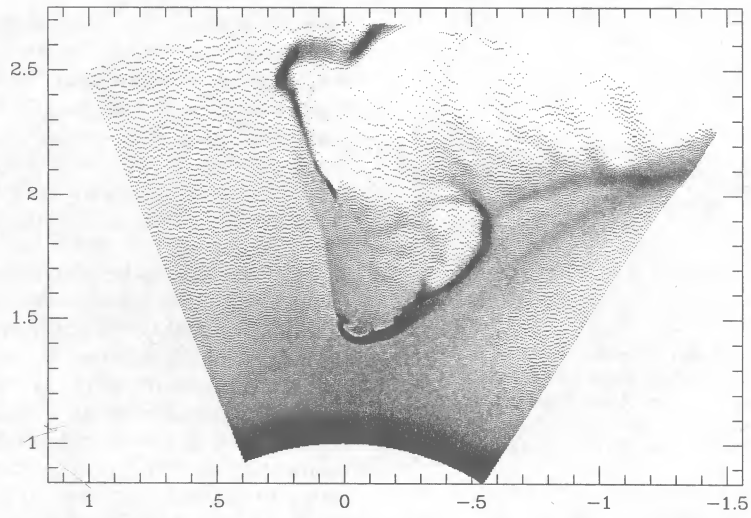

FIG. 9.—Same as Fig. 5, but for the full simulation including the effects of X-ray heating and cooling. The presence of dense filaments on both sides of the wake is the result of an oscillating disk at small radii. The photoionization wake is barely visible to the right of the accretion wake.

flapping driven by the asymmetry of the accreting wind. The density in these filaments can be as great as 100 times the density in the undisturbed wind. In addition to simple advection with the coasting wind, the local ionization parameter within these dense filaments may drop below ξ_{cr}, exposing the gas to the radiative driving force of the companion star. This effect can be seen in Figure 9, where the filament on the left-hand side has been accelerated by the radiation pressure, while the surrounding wind continues to coast. We note, however, that the radiative acceleration of the disturbed portion of the wind (i.e., the reaccelerated filaments) is not well treated by the Sobolev approximation, which assumes a monotonically increasing wind velocity at smaller radii. The photoionization wake caused by the Strömgren zone (see § III*b*), although very weak, can be seen distinct from the accretion wake. This wake pales in comparison with the accretion wake, and contributes only weakly to the total absorption column density. Figure 11 shows the column density profile at several different times, along with an average over several flow times, which smooths over the rapidly changing structure. Although strong absorption is more likely to be seen at late phases, $\phi_{orb} \sim 0.7$, it can occur as early as $\phi_{orb} \sim 0.3$. The strong time-dependent behavior of the accretion wake will result in abrupt changes in the phase profile on time scales $r_{acc}/v_{rel} \ll P_{orb}$.

The time variability of the full model is displayed in Figure 12, which shows six "snapshots" in time separated by 2×10^4 s, substantially shorter than the orbital period of 8×10^5 s. The oscillation period of the bow shock is roughly 9×10^4 s, or ~ 10 flow times. This is slightly longer than the oscillation time seen in the simulation of FT for $\epsilon_\rho = 0.0625$. This difference arises in the slightly longer residence time in the accretion disk phase in our simulations. The transition from one disk phase to the next appears to be triggered when the accretion column feeding the disk is pushed back (away from the companion) by the wind far enough that the accretion column crosses the face of the compact object and begins feeding a disk from the back side rather than from the front (see Fig. 10). This changing flow pattern is in contrast to the stable accretion flow seen in the

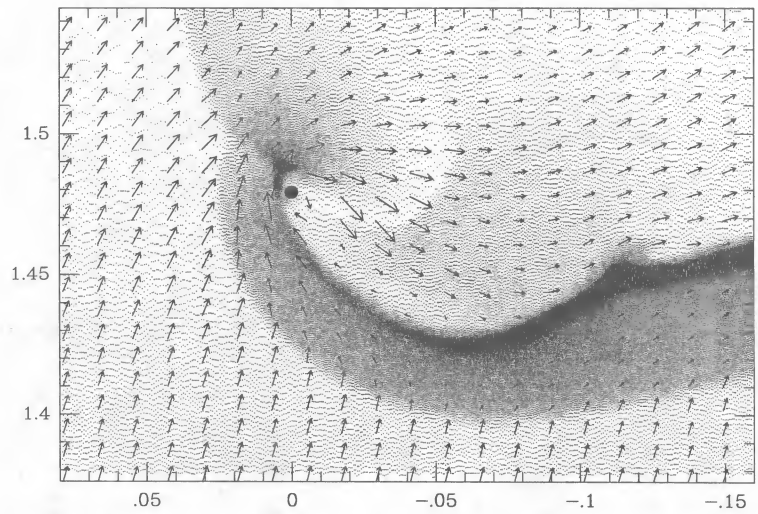

FIG. 10.—Same as Fig. 6, but for the full simulation shown in Fig. 9. The maximum velocity corresponds to 1.4×10^8 cm s^{-1}. The overall density behind the bow shock is lower than in Fig. 6 owing to the lower Mach number in this simulation.

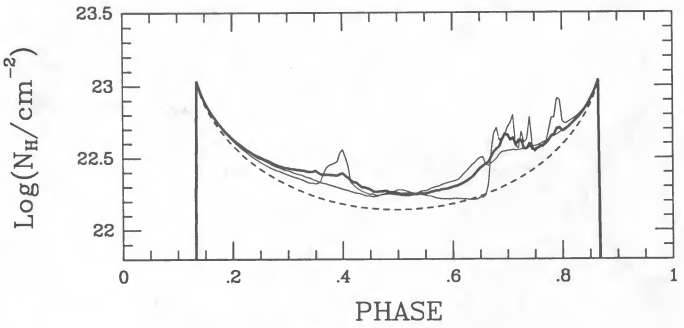

FIG. 11.—Integrated column density for the full simulation shown in Fig. 9. The heavy solid line is an average over 10 flow times across an accretion diameter. The thin solid lines are examples of the column density at different times, showing the magnitude of the variation possible in this time-dependent flow. The dashed line is the column density expected for a spherically symmetric, undisturbed wind.

adiabatic simulation. The difference between these two flows appears to be dominated by the presence of a stationary spiral shock in the adiabatic simulation, while the corresponding shock in the full simulation moves away from the compact object along the side of the accretion column. After this shock has traveled sufficiently far away, the gas on the back side of the accretion column near the compact object is preshock, supersonic flow moving parallel to the accretion column rather than postshock, high-pressure gas. In this case there is no longer sufficient pressure perpendicular to the accretion column to balance the ram pressure of the wind. This difference between the adiabatic and full simulations is consistent with the presence of Compton cooling, which removes thermal energy from the gas behind the spiral shock, allowing the flow to push the spiral shock away from the compact object. Note that this argument is basically independent of the spiral shock: the key is that Compton cooling lowers the thermal pressure that is trying to balance the ram pressure of the wind.

The oscillating behavior of the accretion disk/wake structure is manifested in the time dependence of the mass and angular momentum accreted onto the compact object. The mass accretion rate derived from this simulation as a function of time is shown in Figure 13. In order to avoid problems with our poor resolution at small radii, we have computed the accretion rates as the flux across a circle of radius $r = 2 \times 10^{10}$ cm, which is much less than r_{acc} but larger than the inner radius of our grid. The expected mass accretion rate, based on the two-

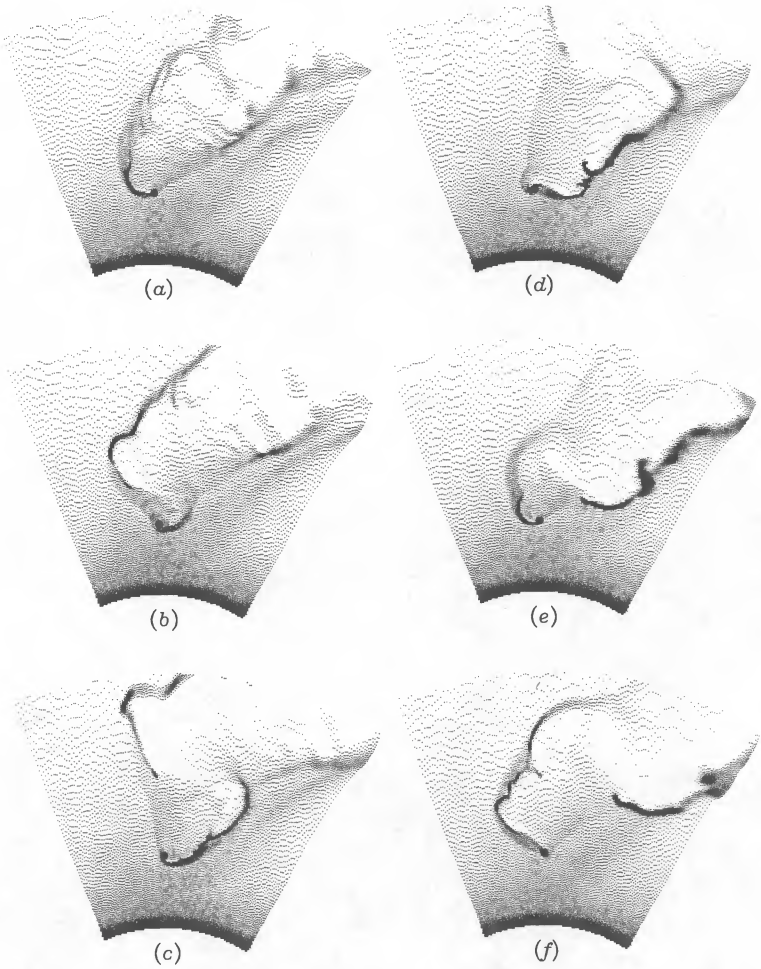

FIG. 12.—(*a–f*) Time series of density plots for the full simulation shown in Fig. 9. Each image is separated by ~2 flow times, beginning ~8 flow times from the start of the simulation. The filaments in the accretion wake can be followed as they are advected off the grid.

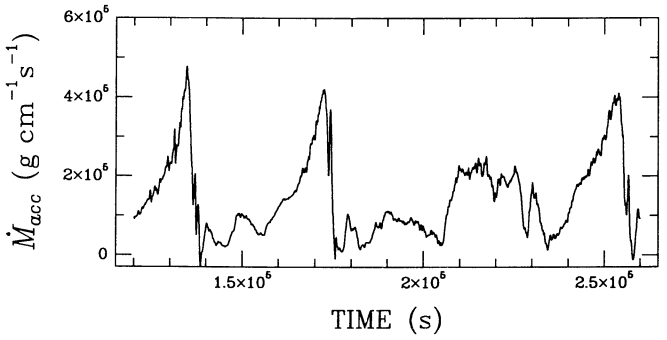

FIG. 13.—Time variability of the mass flux across a circle of radius 2×10^{10} cm for the standard model. The peaks in the mass accretion rate, $\dot{M}_{acc}$, correspond to episodes of disk oscillation, when the acccretion disk changes its sense of rotation.

dimensional version of equation (1), is

$$\dot{M}_{2d} \approx \frac{2r_{acc}\dot{M}_w}{4\pi D^2} . \quad (6)$$

For an accretion radius of 2×10^{11} cm, this estimate gives $\dot{M}_{2d} \approx 5 \times 10^5$ g cm^{-1} s^{-1}. The time-averaged mass accretion rate, $\langle \dot{M}_{acc} \rangle$ is lower than this value by a factor of ~ 3, although the instantaneous value of $\dot{M}_{acc}$ does reach the theoretical estimate during the "flare" events corresponding to a change in disk rotation (see TF, FT). The variation in the angular momentum accretion rate with time, shown in Figure 14, possesses the same quasi-periodic behavior as seen in the mass accretion rate, reflecting the oscillation in the direction of disk rotation. The time evolution shows distinct evidence for a period of $\sim 3.8 \times 10^4$ s, although the variation is not periodic. For example, no direct disk is formed at $\sim 2 \times 10^5$ s as would be expected in a periodic flow. Instead, the flow remains counterrotating for an additional 6×10^4 s, after which the "quasi-periodic" behavior resumes. This temporal behavior is typical of our simulations: a reasonably well-defined time scale, but no coherence over more than a few oscillations. The magnitude of the specific angular momentum, scaled in units of $(v_{rel} r_{acc})$, is expected to be on the order of the density and velocity asymmetries (Ho 1989; FT; TF; Ho *et al.* 1989). The average specific angular momentum during the disk phases in the standard model, $|j| \sim 0.15$, is comparable to ϵ_ρ, although we note that the angular momentum changes sign, a feature not predicted by the analytic perturbation theory.

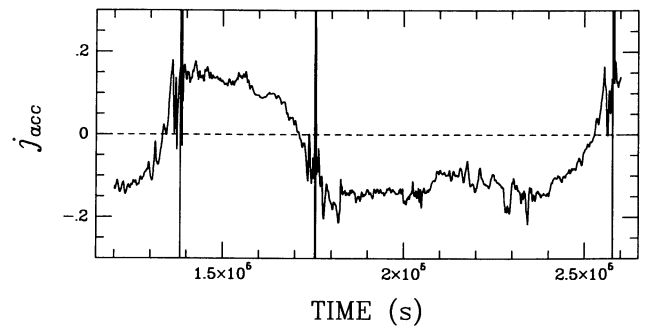

FIG. 14.—Specific angular momentum of the mass transported across a circle of radius 2×10^{10} cm in units of $(r_{acc} v_{rel})$ as a function of time for the standard model.

e) Parameter Dependence

The results of the full simulation described in the preceding subsection will undoubtedly depend on the parameters we have chosen. Unfortunately, we do not have the resources to do an extensive parameter survey covering the many geometric parameters, e.g., R_*, D, P_{orb}, β, v_∞, and so on. Aside from these "system" parameters, the two most important parameters for determining the flow behavior as described in this paper are q, which gives the relative wind velocity at the compact object and the size of the photoionization wake, and L_x, which determines the magnitude of X-ray heating. The heating and cooling times scale with $\dot{M}_w$, and present a third parameter when these time scales are comparable to the flow time. The two parameters, q and L_x, represent the aspects of the wind accretion problem which we understand least well: the effects of X-ray ionization on the radiation pressure force, and the flow close to the compact object and the conversion of accreted mass into X-ray luminosity. With the advantage of an accurate, self-consistent ionization and radiative transfer calculation, we could determine the appropriate value of ξ_{cr}, from which we could obtain q using equation (4). Similarly, if we could self-consistently determine L_x as a function of the mass accretion rate onto the compact object, the entire problem would be set solely by the "system" parameters.

We have attempted a limited study of this two-parameter (q, L_x)-space of MXRBs by varying the X-ray luminosity relative to the wind mass-loss rate while holding the critical ionization parameter at $\xi_{cr} = 10^{2.5}$ ergs cm s^{-1}. In this case, an increase in $L_x/\dot{M}_w$ will both decrease q and increase the effects of X-ray heating. The results of four simulations with $\dot{M}_w = 6.88 \times 10^{-6} M_\odot$ yr^{-1} and increasing values of L_x are shown in Figure 15, and the relevant flow parameters are presented in Table 2. As the size of the Strömgren zone increases, the wind velocity at the compact object decreases, producing a clear trend of increasing accretion radius with increasing $L_x/\dot{M}_w$ in the first three models shown in Figure 15. This, together with the lower Mach number of the wind from higher temperatures and slower velocities, leads to a much wider accretion bow shock. The increased time scales, $t_{fl} = 2r_{acc}/v_{rel}$, are also evident in these simulations, with a much slower flapping of the accretion wake at the higher X-ray luminosities. Aside from this change in time scales, the time behavior of the first two simulations appears qualitatively similar: a quasi-periodic oscillation of the accretion column on either side of the compact object. The third simulation appears similar, except that the dense filaments of the accretion wake appear only on the low-density, high-velocity side. The episodic behavior of the wake is still evident, but it appears that a counterrotating disk is unable to form. Because the standard run (Fig. 12), which differs from this run only in a slightly lower ($\times 0.55$) density, retains the oscillating disk behavior, we postulate that this inability to form a counter disk is the result of stronger radiative cooling than in the standard run.

At very high X-ray luminosities there appears to be a sharp transition in the flow behavior, as shown by the fourth simulation in Figure 15. At this high X-ray luminosity, only a factor of 1.64 higher than in Figure 15*c*, X-ray heating is sufficient to maintain a relatively low Mach number wind, $\mathcal{M} \sim 2.0$. Behind the bow shock the slower velocities and high X-ray flux allow enough time for Compton heating/cooling to maintain an almost isothermal accretion behind the shock. This rapid removal of thermal energy within the bow shock allows the

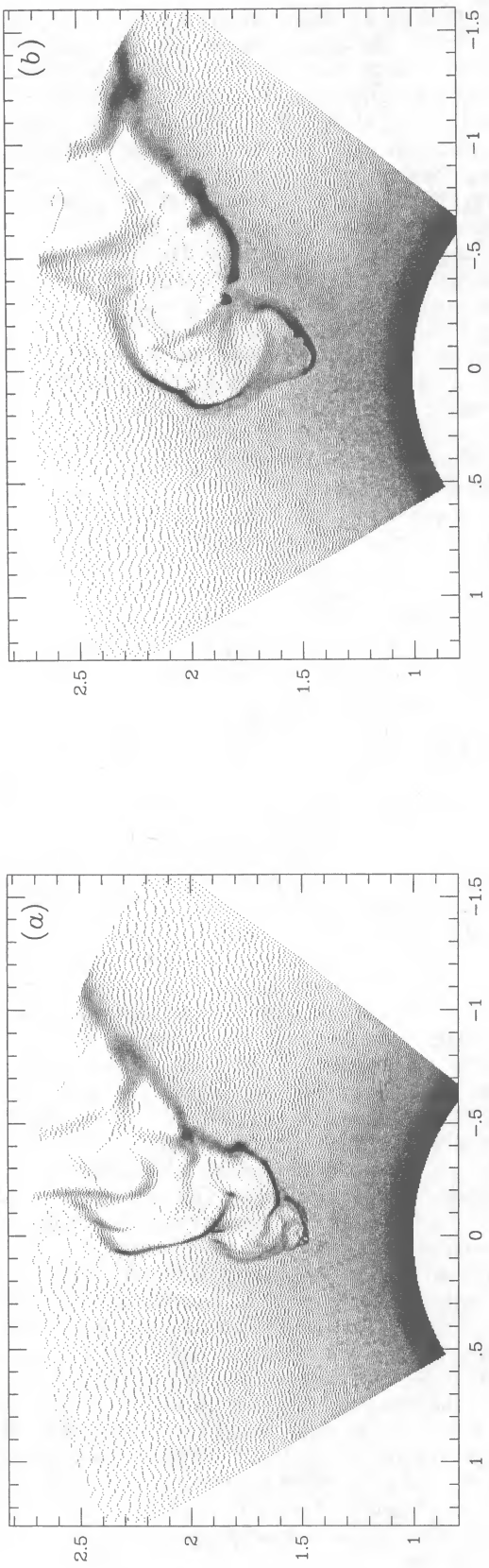

FIG. 15.—Series of four simulations with increasing X-ray luminosity. The wind mass-loss rate is $\dot{M}_w = 6.88 \times 10^{-6}\ M_\odot\ \mathrm{yr}^{-1}$, and the X-ray luminosity, in units of 10^{36} ergs s^{-1}, is (*a*) 2.5, (*b*) 5.0, (*c*) 9.1, and (*d*) 15.0. A clear trend of increasing size of the accretion wake is seen in (*a*)–(*c*), corresponding to the larger accretion radius and longer flow times. The compression of the wind in a photoionization wake is seen in (*c*) and dominates the wind in (*d*). The small clumps near the surface of the primary in (*d*) may be the result of numerical instability in the vicinity of the sonic radius of the accelerating wind. These clumps disperse before reaching the accretion shock, however, and do not appear to influence the remainder of the flow.

TABLE 2

ACCRETION PARAMETERS

L_x (10^{36} ergs s^{-1})	q	v_{rel}[a] (km s^{-1})	r_{acc}[a] (10^{11} cm)	θ_{acc}[a]	t_{fl} (10^3 s)	$\mathcal{M}_{bow}$	$\langle \dot{M}_{acc} \rangle$[b] ($10^5$ g cm^{-1} s^{-1})	$\dot{M}_{2d}$[c] (10^5 g cm^{-1} s^{-1})
0.0	∞	740	0.7	11°	0.9	30.0	1	3.5
2.5	29.4	600	1.0	16	3.3	5.5	2	5
5.0	11.7	490	1.5	19	6.1	3.5	4	7.5
9.1	6.4	430	2.0	21	9.3	2.5	3	10
15.0	3.9	330	3.4	28	20.6	2.0	9	17

[a] These values are obtained at the location of the compact object from simulations with the same q but no gravity of the compact object.

[b] The calculated $\langle \dot{M}_{acc} \rangle$ is an estimate based on only ~ 8 measurements per simulation, and is therefore only a rough gauge of the true time average of $\dot{M}_{acc}$.

[c] Estimated two-dimensional accretion rate using eq. (6) in the text.

flow to approach pure radial accretion, as in an axisymmetric flow with a totally absorbing inner boundary. The resulting accretion bow shock remains surprisingly steady, without the strong flapping seen in lower L_x simulations. There is only a slight density enhancement in the accretion shock, and most of the column density increase is due to the photoionization wake that becomes very pronounced for such a low value of q.

To confirm the dependence of this steady flow on Compton cooling, we ran another simulation with the same L_x and $\dot{M}_w$ as in Figure 15*d*, but with a larger value of q, $q = 11.7$, corresponding to the simulation in Figure 15*b*. The accretion wake was again very steady, as in the previous high X-ray luminosity run. The only differences were a weaker photoionization wake owing to the larger q and a slightly narrower accretion wake as a result of the larger Mach number (larger $q \rightarrow$ higher v_w at the compact object).

The different modes of behavior observed in our simulations of MXRBs appear to be controlled by Compton heating and cooling of the accreting wind near the compact object. In the adiabatic flow with large accretion radius (Fig. 5) the absence of any cooling produced a high-pressure region around the compact object that appeared to prevent any disk oscillations, and the accretion column remained on the high-density side of the asymmetric wind feeding a counterrotating disk. At moderate X-ray luminosities, X-ray heating and radiative cooling conspired to produce a quasi-periodic oscillation between a counter- and a direct-rotating disk, similar to the behavior seen in FT and TF. As the X-ray luminosity increased, only a direct disk was occasionally seen to form, while at high X-ray luminosity Compton cooling was sufficiently fast to maintain a steady state radial accretion flow inside the bow shock without any disk structure. Because the asymmetry in this series varied by only a factor of ~ 2, and because the check on the high-luminosity run with higher q showed that the observed changes were a function of L_x, we think that this trend in behavior is due to the increasing X-ray luminosity rather than to changes in the asymmetry of the accreting wind.

Because the Compton cooling time depends only on the local X-ray flux, L_x/r^2, while the size of the Strömgren zone also depends on ξ_{cr}, the exact value of q when Compton cooling suppresses the accretion wake oscillations will depend on the appropriate value of ξ_{cr}. Thus, the relative importance of X-ray heating/cooling with respect to the size of the X-ray Strömgren zone will be shifted up (down) for higher (smaller) values of the critical ionization parameter.

The time-averaged mass accretion rate onto the compact object is proportional to the expected rate given by equation (6), although it is consistently smaller than the predicted rate by a factor of ~ 2. In the first three simulations, $\dot{M}_{acc}$ oscillates by an order of magnitude, with the peaks occurring when the accretion disk changes its sense of rotation (see Fig. 13). In the high-L_x run, $\dot{M}_{acc}$ settles down to a relatively steady value of 9×10^5 g cm^{-1} s^{-1}, compared with the estimated total mass flux crossing the accreting diameter, 1.7×10^6 g cm^{-1} s^{-1}. The angular momentum accretion rate follows the oscillating behavior shown in Figure 14 for the two low-L_x simulations. The intermediate simulation of Figure 14*c* displays similar fluctuations in the mass accretion rate, but the specific angular momentum always remains positive, reflecting the fact that a counterrotating disk never forms. The high-L_x run is characterized by low, relatively constant accretion of (positive) specific angular momentum with a value of $j \approx 0.01$.

IV. DISCUSSION

a) X-Ray Absorption

Real MXRBs exhibit variability in their X-ray spectra and luminosity on time scales ranging from pulsar periods ($\sim$seconds or less) to the total time over which they have been observed (~ 10 yr). In spite of this complexity one of the most apparent behaviors is the systematic increase in photoelectric absorption (as inferred from the "hardness" of the X-ray spectrum) observed during the later half of the orbital period. This is indicative of material trailing the X-ray source in its orbit. The column density enhancements, in addition to that observed at earlier orbital phases, are generally of order 10^{23} cm^{-2}. For example, in Vela X-1 (4U 0900−40) the enhancement is $\simeq 2 \times 10^{23}$ cm^{-2} (Charles *et al.* 1978; see also Sato *et al.* 1986). A similar enhancement is observed in 4U 1700−37 (White, Kallman, and Swank 1983; Haberl, White, and Kallman 1989). The absorption increase is most apparent when observations of several binary orbits are averaged together; observations of a single orbit may find this effect weaker or stronger than average. In addition, high-resolution spectra of Vela X-1 (4U 0900−40) detected absorption edges near 2 and 2.5 keV at phase 0.8, indicative of silicon and sulfur, which suggest a much greater ($\sim 10^{23}$ cm^{-2}) column density of partially ionized material trailing the compact object (Kallman and White 1982).

The results shown in the previous section are generally consistent with the observed properties of Vela X-1 (4U 0900−40) for the fiducial model parameters. As shown in Figure 11, the model with X-ray heating and ionization provides column densities of up to 10^{23} cm^{-2} near phase 0.7. The absorption of

X-rays in the accretion wake is predicted to be variable on a time scale of ~ 1 hr, the flow time across the accretion radius. The absorption of X-rays in the photoionization wake is not seen to vary significantly in our models, although dynamical instabilities driven by changes in ionization may alter this result. Although the variability behavior of the X-ray flux and absorbing column from most MXRBs has not been thoroughly studied on such time scales, the model variability is not inconsistent with observed variability behavior. The results of our models show that the full 10^{23} cm^{-2} column excess appears at orbital phases around ~ 0.7. For systems with small values of q, our simulations suggest that the photoionization wake can enhance $N_{\rm H}$ at even later phases. It is important to note that three-dimensional flows will probably produce higher densities in the filaments than are provided by our models, owing to the additional compression in the third dimension.

b) *Mass Accretion Rate*

In spite of the fact that the large-scale wake structures differ greatly from the uniform flow assumed in the simple wind accretion picture of Davidson and Ostriker (1973), the mass accretion rates we derive are crudely consistent with the estimates of equation (6). Table 2 gives the time-averaged mass accretion rate, $\langle \dot{M}_{\rm acc} \rangle$, produced by each of the four simulations in which all of the relevant physical effects were included. For comparison, an estimate of the two-dimensional mass accretion rate using equation (6) is also provided in Table 2. We find that the two mass accretion rates, $\langle \dot{M}_{\rm acc} \rangle$ and $\dot{M}_{\rm 2d}$ are proportional to within 50% over the range of parameters spanned by our models. This suggests that the estimate given by equation (1), although very simplistic, provides a reasonable measure of the expected time-averaged mass accretion rate in MXRBs. Although the large-scale structure of the flow is highly sensitive to the conditions near the compact object, i.e., the effective adiabatic index and the Mach number, the time average of the mass flow across the innermost boundary of the grid is much less so. In all but the highest luminosity simulation, the mass accretion rate fluctuated over an order of magnitude with time in our models. This temporal behavior will be reflected in variations of the accretion-driven luminosity. Although other processes not considered here will contribute to the time variability of L_x, we expect the short time scale variability in $\dot{M}_{\rm acc}$ predicted by our simulations to produce abrupt changes in L_x on time scales as short as 10^3 s.

c) *Angular Momentum Accretion Rate*

Pulsations from compact X-ray sources are a useful probe of a great variety of quantities of interest in the study of MXRBs, including the equation of state of nuclear matter, orbital velocity and binary separation, and inhomogeneities in the stellar wind. As shown by MIS, FT, and TF, and in Figure 14, the variability of the flow on length scales comparable to the binary separation is accompanied by large variations in the angular momentum accretion rate. These changes occur on time scales as short as the flow time across the accretion radius, which is $\sim 10^3$ s in our standard model. We can estimate the angular momentum accretion rate in a three-dimensional flow by multiplying the specific angular momentum observed in our simulations by the expected mass accretion rate. Based on a typical (normalized) specific angular momentum in the accreting gas of $|j| \sim 0.15$ in our standard model, we predict an angular momentum accretion rate of $|\dot{J}| \simeq 4 \times 10^{34}$ g cm^2 s^{-2} during a "disk phase." Assuming a moment of inertia for a neutron star of $I = 10^{45}$ g cm^2, this would produce a pulse period change of $\dot{P}/P = P\dot{J}/2\pi I \simeq 6 \times 10^{-2}$ yr^{-1} for 4U 0900−40 (Vela X-1), even higher than the peak observed pulse period changes in this system (Boynton *et al.* 1984). Note, however, that Boynton *et al.* did not resolve the shortest time scale changes, which must therefore be on times less than 2–3 days. The long-term variation of P in Vela X-1 is more than an order of magnitude smaller than the observed short time scale variability ($\dot{P}/P \simeq 2 \times 10^{-4}$ yr^{-1} from 1979 to 1981; Boynton *et al.* 1984). We cannot predict any secular changes in $\dot{J}$ over many flow times, primarily because we would need to run the simulations over a very long time in order to average out the oscillations of the accretion disk. Based on the wide range of behavior seen in our simulations, we do not doubt that both secular increases and decreases in P can occur in wind-accretion X-ray pulsars. Along with the time variability predicted by our models, the fluctuations in $\dot{J}$ in real MXRBs are likely to be affected by other processes not considered in this paper, e.g., inhomogeneities in the stellar wind which are not associated with X-ray ionization effects. In addition, we have not attempted to model the transfer of mass and angular momentum from the inner radius in our simulation (corresponding to the outer radius of an accretion disk) through the accretion disk and onto the compact object, nor have we considered the feedback of $\dot{M}_{\rm acc}$ on L_x, which should enhance the time variability. In any case, our simulations show that large amounts of angular momentum can be accreted with both positive and negative sign, and that fluctuations in $\dot{J}$ are expected on time scales as short as 10^3 s. We point out that MIS came to the same conclusions. The changes in P associated with the fluctuations of accreted angular momentum seen in our models should persist and would be detectable by future large-area X-ray timing experiments.

d) *Eclipse Behavior*

One consequence of the wake structures predicted by our models is the existence of a large volume ($\sim 10\%$ of the total wind) of gas at temperatures $\geq 10^6$ K. This gas will emit diffuse X-rays via bremsstrahlung, collisions, and recombination and will scatter the X-rays emitted from the compact object. The density in the hot gas is approximately 10^{-3} of that in the rest of the wind, its emission measure is EM $\simeq 2.9 \times 10^{58} \dot{M}_6^2 v_8^{-2}$ ergs s^{-1}, and its luminosity is $L_{\rm diff} \approx 2.2 \times 10^{33} \Lambda_{22}$ ergs s^{-1} for our fiducial choice of parameters, where Λ_{22} is the emissivity of the gas in units of 10^{-22} ergs cm^3 s^{-1}. This is comparable to the luminosity expected from the intrinsic emission of the primary, but will be distinguishable by its much harder spectrum. The diffusely emitted iron K line will be near 6.7–6.8 keV, owing to the high ionization of the hot gas, and so will be distinguishable from the iron emission from the rest of the wind. Furthermore, the diffuse emission will have a distinctive orbital phase dependence, becoming most apparent at late phases after the compact object is eclipsed. As the compact object emerges from eclipse, the diffuse emission, which trails the compact object in orbital phase owing to the Coriolis force, will be near the maximum of its own (partial) eclipse.

Scattering will reflect $\simeq 1\%$–10% of the X-rays from the compact object into the observer's line of sight. The luminosity and intrinsic spectrum of these X-rays is not strongly dependent on the existence of wake structures trailing the compact object, so that they are likely to be observable only during the eclipse of the compact object. Scattered X-rays differ from direct X-rays in the amount of photoelectric absorption they suffer as they escape the wind. In the absence of wake struc-

tures, scattered X-rays travel a longer path through the wind to the observer, but at greater distances from the surface of the primary. Since the wind density is a strongly decreasing function of distance from the primary surface, scattered X-rays will in general suffer less absorption than direct X-rays. Wakes of hot gas will enhance this effect, since the gas in the wakes will have a lower ratio of photoelectric opacity to scattering opacity than the rest of the wind. The X-ray spectrum of Vela X-1 during eclipse is observed to be softer than that away from eclipse (Nagase *et al.* 1984), consistent with this idea.

e) X-Ray Reprocessing

Effects of mass loss in massive stars appear most clearly in the ultraviolet *P* Cygni (resonance) lines of ions such as N v, Si iv, and C iv. McCray and Hatchett (1975) and Hatchett and McCray (1977) predicted that the ionization of the stellar wind by an X-ray source should be observable as a marked orbital phase dependence of the *P* Cygni profiles of the lines of these ions. This effect has been clearly demonstrated to occur in the source Vela X-1 (4U 0900−40/HD 77581) using both high- and low-resolution *IUE* observations (Dupree *et al.* 1978; Hammerschlag-Hensberge 1980). The effect has also been observed at low resolution in the Cyg X-1, SMC X-1, and LMC X-4 systems (see Hammerschlag-Hensberge 1980 for a review) and at high resolution in SMC X-1 (Hammerschlag-Hensberge, Kallman, and Howarth 1984). The shapes of the observed line profiles are crudely consistent with those predicted by model calculations based on the assumption of a spherical wind (McCray *et al.* 1984; Hammerschlag-Hensberge, Howarth, and Kallman 1990), but the models fail to reproduce some of the observed narrow profile features. Wake structures are likely to affect the observed profiles strongly near phase 0.5, and so may explain some of the discrepancies. We plan to present such models in a future paper.

f) Limitations of the Models

The results obtained from our numerical simulations are based upon a number of simplifying assumptions that were made in order to make the calculation of the accretion flow tractable. As a consequence, the results should be regarded as indicative of the type of flow structures expected when the additional physics associated with X-ray photoionization and X-ray heating and cooling are included. The specific parameters characterizing each simulation should not be directly associated with a particular X-ray source, since the limitations of the models make them somewhat uncertain. In particular, the most important limitation regarding the flow morphology is the restriction of the flow to two dimensions in the orbital plane. The convergence of the flow into the orbital plane is important, especially if the stellar wind is not confined to this plane. Its inclusion may tend to reduce the effect of the nonsteady behavior and introduce other asymmetries which have not been incorporated into the model. The focusing of the wind in the third dimension will also enhance the density of the accreting material at small radii, which may increase the observed column density in the filaments of the accretion wake and decrease the radiative cooling time. Within the context of the assumed input physics, the optical depth effects in the He ionization zone need to be included to determine whether the trace elements responsible for the accretion of the wind survive (see Masai 1984). Such effects complicate the problem as the determination of the Strömgren zone becomes a function not only of the ionization parameter, ξ, but also of the optical depth. The further assumption of constant X-ray luminosity also restricts the applicability of the result. It is very likely that the relaxation of this assumption will lead to more temporal variability (see Ho and Arons 1987*b*). Finally, for the highest X-ray luminosities, the effect of X-ray radiation pressure on the hydrodynamics of the flow will need to be incorporated. Studies along these lines are necessary and will be the subject of future investigations.

V. SUMMARY

We have investigated the effects of a compact companion on the radiatively driven stellar wind of an OB star in a massive X-ray binary system. To this end we have presented two-dimensional numerical simulations in which the X-ray luminosity photoionizes an X-ray Strömgren zone around the compact object. Within this ionized zone the wind is no longer accelerated by the radiation flux of the OB primary. The resulting decrease in wind velocity at the compact object leads to both a larger accretion radius and a photoionization wake trailing behind the Strömgren zone where the slower wind is overtaken by the unaffected wind.

For moderately strong X-ray sources ($L_x \sim 10^{36}$ ergs s^{-1}), our simulations are characterized by a time-dependent accretion wake containing dense filaments of compressed gas. The variability seen in the accretion wake at large radii is correlated with an oscillating accretion disk that produces episodic changes in the mass accretion rate and in the sign of the accreted angular momentum. The compression of gas in the accretion wake can produce densities approaching 100 times the density in the undisturbed wind. The column density in this wake can approach 10^{23} cm^{-2}, sufficiently large enough to contribute to the photoelectric absorption of X-rays. The time scale associated with the fluctuations in the wake is shorter than the orbital period, suggesting that the absorption column density as a function of orbital phase will differ from orbit to orbit. At higher X-ray luminosities ($L_x \gtrsim 10^{37}$ ergs s^{-1}) Compton cooling near the compact object keeps the flow roughly isothermal, and the accretion is more nearly radial. In this case the accretion flow becomes steady and the column density in the accretion wake is relatively small. The photoionization wake becomes very pronounced, however, and could enhance the column density at late orbital phases all the way into eclipse.

This work suggests that the photoelectric absorption seen in several MXRB systems at late orbital phases can be explained by the presence of dense filaments in an accretion wake around the compact object and/or by the presence of a photoionization wake created by the ionizing effects of the X-ray luminosity. Our simulations also point to episodic behavior in the mass accretion rate which should be reflected in changes in the accretion-driven X-ray luminosity on a time scale of hours (see also MIS; Taam and Fryxell 1988). Similar fluctuations are expected in the spin-up/spin-down of X-ray pulsars in MXRBs as a result of changes in the sign and magnitude of the accreted angular momentum.

This work was supported in part by the NASA Astrophysics Theory Program under grant NAGW-768 and the National Science Foundation under grant AST-8608291. The numerical simulations were computed on the Cray X-MP/48 at the National Center for Supercomputing Applications at the University of Illinois at Urbana-Champaign. One of us (J. M. B.) gratefully acknowledges helpful discussions with Ian Stevens and Stan Owocki.

APPENDIX

The two-dimensional nonrelativistic gasdynamical equations for conservation of mass, momentum (in r and in ϕ), and energy in the equatorial plane of a spherical coordinate system are expressed as

$$\frac{\partial \rho}{\partial t} + \frac{1}{r^2}\frac{\partial}{\partial r}(r^2 \rho v_r) + \frac{1}{r}\frac{\partial}{\partial \phi}(\rho v_\phi) = 0 , \tag{A1}$$

$$\frac{\partial}{\partial t}(\rho v_r) + \frac{1}{r^2}\frac{\partial}{\partial r}(r^2 \rho v_r^2) + \frac{1}{r}\frac{\partial}{\partial \phi}(\rho v_r v_\phi) = -\frac{\partial P}{\partial r} + \frac{\rho v_\phi^2}{r} + \rho g_* + \rho g_{\mathrm{co},r} + \mathscr{F}_{\mathrm{rad}} , \tag{A2}$$

$$\frac{\partial}{\partial t}(\rho v_\phi) + \frac{1}{r^2}\frac{\partial}{\partial r}(r^2 \rho v_r v_\phi) + \frac{1}{r}\frac{\partial}{\partial \phi}(\rho v_\phi^2) = -\frac{\partial P}{\partial \phi} - \frac{\rho v_r v_\phi}{r} + \rho g_{\mathrm{co},\phi}, \tag{A3}$$

$$\frac{\partial}{\partial t}(\rho \mathscr{E}) + \frac{1}{r^2}\frac{\partial}{\partial r}[r^2 v_r(\rho \mathscr{E} + P)] + \frac{1}{r}\frac{\partial}{\partial \phi}[v_\phi(\rho \mathscr{E} + P)] = \rho v_r(g_* + g_{\mathrm{co},r}) + \rho v_\phi g_{\mathrm{co},\phi} + n^2(\Gamma - \Lambda) , \tag{A4}$$

where $\mathscr{E} = 0.5v^2 + (\gamma - 1)^{-1}P/\rho$ is the total specific energy, g_* is the gravitational force of the primary star, g_{co} is the gravitational force of the compact object, and the subscripts r and ϕ refer to the radial and azimuthal components, respectively. Other symbols are as defined in the text.

REFERENCES

Abbott, D. C. 1982, *Ap. J.*, **259**, 282.
Bondi, H., and Hoyle, F. 1944, *M.N.R.A.S.*, **104**, 273.
Boynton, P. E., Deeter, J., Lamb, F. K., Zylstra, G., Pravdo, S. H., White, N. E., Wood, K., and Yentis, D. J. 1984, *Ap. J. (Letters)*, **283**, L53.
Branduardi, G., Mason, K. O., and Sanford, P. W. 1978, *M.N.R.A.S.*, **185**, 137.
Buff, J., and McCray, R. A. 1974, *Ap. J.*, **189**, 147.
Castor, J. I., Abott, D. C., and Klein, R. I. 1975, *Ap. J.*, **195**, 157.
Charles, P. A., Mason, K. O., White, N. E., Chane, J. L., Sanford, P. W., and Moffatt, A. J. F. 1978, *M.N.R.A.S.*, **183**, 813.
Collela, P., and Woodward, P. R. 1984, *J. Comput. Phys.*, **54**, 174.
Conti, P. S. 1978, *Astr. Ap.*, **63**, 225.
Cowie, L. L., Ostriker, J. P., and Stark, A. A. 1978, *Ap. J.*, **226**, 1041.
Davidson, K., and Ostriker, J. P. 1973, *Ap. J.*, **179**, 588.
Dupree, A. K., *et al.* 1978, *Nature*, **275**, 400.
Fransson, C., and Fabian, A. C. 1980, *Astr. Ap.*, **87**, 102.
Friend, D. B., and Abbott, D. C. 1986, *Ap. J.*, **311**, 701.
Friend, D. B., and Castor, J. I. 1982, *Ap. J.*, **261**, 293.
Fryxell, B. A., and Taam, R. E. 1988, *Ap. J.*, **335**, 862 (FT).
Fryxell, B. A., Taam, R. E., and McMillan, S. L. W. 1987, *Ap. J.*, **315**, 536 (FTM).
Haberl, F., White, N. E., and Kallman, T. R. 1989, *Ap. J.*, **343**, 409.
Hammerschlag-Hensberge, G. 1980, in *Proc. Second European IUE Conf.* (ESA SP-157), p. lix.
Hammerschlag-Hensberge, G., Howarth, I. D., and Kallman, T. R. 1990, *Ap. J.*, **352**, 698.
Hammerschlag-Hensberge, G., Kallman, T. R., and Howarth, I. D. 1984, *Ap. J.*, **249**, 253.
Hatchett, S. P., Buff, J., and McCray, R. A. 1976, *Ap. J.*, **206**, 847.
Hatchett, S. P., and McCray, R. A. 1977, *Ap. J.*, **211**, 552.
Ho, C. 1989, *M.N.R.A.S.*, **236**, 299.
Ho, C., and Arons, J. 1987*a*, *Ap. J.*, **316**, 283.
———. 1987*b*, *Ap. J.*, **321**, 404.
Ho, C., Taam, R. E., Fryxell, B. A., Matsuda, T., Kaide, H., and Shima, E. 1989, *M.N.R.A.S.*, **228**, 1447.
Hoyle, F., and Lyttleton, R. A. 1939, *Proc. Cambridge Phil. Soc.*, **35**, 405.
Hunt, R. 1971, *M.N.R.A.S.*, **154**, 141.
Jackson, J. C. 1975, *M.N.R.A.S.*, **172**, 483.
Kallman, T. R., and McCray, R. 1982, *Ap. J. Suppl.*, **50**, 263.
Kallman, T. R., and White, N. E. 1982, *Ap. J. (Letters)*, **261**, L35.
Klein, R. I., and Castor, J. I. 1978, *Ap. J.*, **220**, 902.
Lucy, L. B. 1984, *Ap. J.*, **284**, 351.
Lucy, L. B., and White, R. L. 1980, *Ap. J.*, **241**, 300.
MacGregor, K. B., Hartmann, L., and Raymond, J. C. 1979, *Ap. J.*, **231**, 514.
MacGregor, K. B., and Vitello, P. A. J. 1982, *Ap. J.*, **259**, 267.
Masai, K. 1984, *Ap. Space Sci.*, **106**, 391.
Matsuda, T., Inoue, M., and Sawada, K. 1987, *M.N.R.A.S.*, **226**, 785 (MIS).
McCray, R., and Hatchett, S. 1975, *Ap. J.*, **199**, 196.
McCray, R., Kallman, T. R., Castor, J. I., and Olson, G. L. 1984, *Ap. J.*, **282**, 245.
McCray, R., Wright, C., and Hatchett, S. 1977, *Ap. J. (Letters)*, **211**, L29.
Nagase, F., *et al.* 1984, *Ap. J.*, **280**, 259.
Owocki, S. P., Castor, J. I., and Rybicki, G. B. 1988, *Ap. J.*, **335**, 914.
Owocki, S. P., and Rybicki, G. B. 1984, *Ap. J.*, **284**, 354.
Pauldrach, A., Puls, J., and Kudritzki, R. P. 1986, *Astr. Ap.*, **164**, 86.
Petterson, J. A. 1978, *Ap. J.*, **224**, 625.
Sato, N., *et al.* 1986, *Pub. Astr. Soc. Japan*, **38**, 731.
Savonije, G. J. 1983, in *Accretion Driven Stellar X-Ray Sources*, ed. W. H. G. Lewin and E. P. J. van den Heuvel (Cambridge: Cambridge University Press), p. 343.
Schreier, E. J., Schwartz, J., Giacconi, R., Fabbiano, G., and Morin, G. 1976, *Ap. J.*, **204**, 539.
Shima, E., Matsuda, T., Takeda, H., and Sawada, K. 1985, *M.N.R.A.S.*, **217**, 365.
Stevens, I. R., and Kallman, T. R. 1990, *Ap. J.*, submitted.
Taam, R. E., and Fryxell, B. A. 1988, *Ap. J. (Letters)*, **327**, L73.
———. 1989, *Ap. J.*, **339**, 297 (TF).
Tarter, C. B., Tucker, W. H., and Salpeter, E. E. 1969, *Ap. J.*, **156**, 943.
Wang, Y.-M. 1979, *Astr. Ap.*, **74**, 253.
———. 1981, *Astr. Ap.*, **102**, 36.
Watson, M. G., and Griffiths, R. E. 1977, *M.N.R.A.S.*, **178**, 513.
White, N. E. 1985, in *Interacting Binaries*, ed. P. P. Eggleton and J. E. Pringle (Dordrecht: Reidel), p. 249.
White, N. E., Kallman, T. R., and Swank, J. H. 1983, *Ap. J.*, **269**, 264.
Withbroe, G. 1971, in *The Menzel Symposium on Solar Physics, Atomic Spectra, and Gaseous Nebulae*, ed. K. B. Gebbie (NBS Spec. Pub. 353; Washington, DC: NBS), p. 127.

JOHN M. BLONDIN: Department of Astronomy, University of Virginia, P.O. Box 3818, Charlottesville, VA 22903

BRUCE A. FRYXELL: Department of Physics, University of Arizona, Tucson, AZ 85721

TIMOTHY R. KALLMAN: NASA/Goddard Space Flight Center, Laboratory for High Energy Astrophysics, Code 665, Greenbelt, MD 20771

RONALD E. TAAM: Department of Physics and Astronomy, Northwestern University, Evanston, IL 60208